Sulfation affects apical extracellular matrix organization during development of the *Drosophila* embryonic salivary gland tube

J. Luke Woodward[1,¶], Jeffrey Matthew[1,¶], Rutuparna Joshi[1], Vishakha Vishwakarma[1], Ying Xiao[2], and SeYeon Chung[1,*]

1 Department of Biological Sciences, Louisiana State University, Baton Rouge, LA 70803, USA

2 Shared Instrumentation Facility, Louisiana State University, Baton Rouge, LA 70803, USA

¶ These authors contributed equally to this study.

*Author for correspondence: seyeonchung@lsu.edu

Abstract

The apical extracellular matrix (aECM) plays a critical role in epithelial tube morphogenesis during organ formation, but its composition and organization remain poorly understood. Using the *Drosophila* embryonic salivary gland (SG) as a model, we identify Papss, an enzyme that synthesizes the universal sulfate donor PAPS, as a critical regulator of tube lumen expansion. *Papss* mutants show a disorganized apical membrane, condensed aECM, and disruptions in Golgi structures and intracellular trafficking. SG-specific expression of wild-type Papss, but not the catalytically inactive form, rescues the defects in *Papss* mutants, suggesting that defects in sulfation are the underlying cause of the phenotypes. Additionally, we identify two zona pellucida (ZP) domain proteins, Piopio (Pio) and Dumpy (Dpy), as key components of the SG aECM. In the absence of *Papss*, Pio is gradually lost in the aECM, while the Dpy-positive aECM structure is condensed and dissociates from the apical membrane, leading to a thin lumen. Mutations in *dpy* or *pio*, or in *Notopleural*, which encodes a matriptase that cleaves Pio to form the luminal Pio pool, result in a SG lumen with alternating bulges and constrictions, with the loss of *pio* leading to the loss of Dpy in the lumen. Our findings underscore the essential role of sulfation in organizing the aECM during tubular organ formation and highlight the mechanical support provided by ZP domain proteins in maintaining luminal diameter.

Introduction

Epithelial tubes are critical components of many key biological organs, including the kidney, heart, and lungs. Aberrant tube size leads to common diseases and congenital disorders, such as polycystic kidney disease, asthma, and lung hypoplasia. Tube morphogenesis is regulated by multiple factors, including intracellular mechanisms, intercellular interactions, and interactions between cells and the surrounding extracellular matrix (ECM). Specifically, events at the apical (luminal) surface of a tube play an important role in regulating tube diameter and growth, thereby influencing overall tube shape (Myat and Andrew, 2002). During tubular organ formation, the surrounding epithelium secretes apical ECM (aECM) components into the lumen. These aECM components form the luminal meshwork and interact with the apical membrane, playing a critical role in epithelial morphogenesis and regulation of tube dimensions (Jazwinska et al., 2003; Devine et al., 2005; Luschnig et al., 2006; Wang et al., 2006; Syed et al., 2012; Dong et al., 2014; Drees et al., 2023; Gill et al., 2016; Cohen, Sparacio, et al., 2020).

The aECM has a distinct composition compared to the basal ECM, with a diverse array of components (Zheng et al., 2020). ZP domain proteins, which are highly conserved across species, are of particular interest and are characterized by a conserved 260 amino acid ZP domain that mediates homo- or heteromeric polymerization into filaments. Initially identified in the extracellular coat of mammalian oocytes, ZP domain proteins have been shown to play a critical role in the organization of specialized apical structures in various tissues in species ranging from worms to humans (Porter & Tamm, 1955; Yan et al., 2012; Legan et al., 1997; Op De Beeck et al., 2012; Renner et al., 2007; McAllister et al., 1994; Wong et al., 2000; Cohen, Bermudez, et al., 2020; Plaza et al., 2010; Jovine et al., 2005; Litscher & Wassarman, 2020; Wilkin et al., 2000; Ghosh & Treisman, 2024). Chitin, a biopolymer of N-acetylglucosamine, is another major aECM component that is abundant in invertebrates and some vertebrates (Tang et al., 2015; Mei et al., 2024). In many *Drosophila* and *C. elegans* tissues, chitin forms a network of fibers that provide mechanical support and maintain the integrity of the epithelial layer (Araujo et al., 2005; Devine et al., 2005; Moussian et al., 2006; Tonning et al., 2005; Zhang et al., 2005). Several studies have shown the role of ZP proteins in maintaining the chitin matrix in the aECM. During *Drosophila* tracheal development, two ZP proteins, Dumpy (Dpy) and Piopio (Pio), build an elastic structure in the lumen that modulates mechanical stress and maintains the chitin matrix

63 (Jazwinska et al., 2003; Dong et al., 2014; Drees et al., 2023). In the *Drosophila* corneal lens,
64 another ZP domain protein, Dusky-like, establishes an external scaffold for chitin retention
65 (Ghosh & Treisman, 2024). However, many organs in both vertebrates and invertebrates have a
66 non-chitinous aECM, and the role of ZP proteins in the non-chitinous aECM is less well
67 understood.

68 Post-translational modifications of the aECM are essential for proper tube dimensions
69 during organ formation (Luschnig et al., 2006; Wang et al., 2006; Abrams et al., 2006; Herman
70 & Horvitz, 1999; Hwang et al., 2003). Sulfation is an abundant post-translational modification
71 that takes place in the Golgi apparatus, where a sulfate group is covalently attached to amino
72 acid residues of proteins or side chains of proteoglycans (Gunal et al., 2019). Several studies in
73 *C. elegans* have shown key roles of sulfation in neuronal organization, development of
74 reproductive tissues, and phynotypic plasticitiy, linking this post-translational modification to
75 multiple cellular processes (Turnbull et al., 2003; Bulow & Hobert, 2004; Kinnunen et al., 2005;
76 Tecle et al., 2013; Diaz-Balzac et al., 2014; Dierker et al., 2016). A study in a mouse model of
77 cystic fibrosis also suggest a link between the disease state and proper sulfation levels in organs
78 (Xia et al., 2005), but the role of sulfation in tubular organ development and aECM organization
79 remains elusive.

80 Sulfation reactions require a high-energy form of sulfate, 3'-phosphoadenosine-5'-
81 phosphosulfate (PAPS), which is produced by the enzyme PAPS synthetase (Papss) (van den
82 Boom et al., 2012; Gunal et al., 2019). Mammals have two Papss isoforms, Papss1 and Papss2.
83 *Papss1* shows ubiquitous expression, with higher levels in glandular cells and salivary duct cells,
84 suggesting that high degrees of sulfation are required in these cell types (Uhlen et al., 2005;
85 Karlsson et al., 2021). *Papss2* shows a more restricted expression in certain tissues such as
86 cartilage, and mutations in *Papss2* have been associated with skeletal dysplasia in humans
87 (Faiyaz ul Haque et al., 1998; Ahmad et al., 1998; Kurima et al., 1998; Ford-Hutchinson et al.,
88 2005). Mouse models with exon deletions in *Papss1* or *Papss2* show extensive defects, including
89 lethality (*Papss1*) and abnormal craniofacial and limb morphology (*Papss2*) (Groza et al., 2023),
90 demonstrating that Papss is vital for developmental processes in mammals. *Drosophila* has a
91 single *Papss* gene, allowing for a straightforward investigation of its function in developmental
92 processes without redundancy. By studying the role of *Papss* in *Drosophila* development, we can

93 gain valuable insights into the role of this conserved enzyme in normal development and disease
94 in humans.

95 To understand the role of post-translational modification in aECM organization and to
96 determine the key composition of the non-chitinous aECM in tubular organs, we use the
97 *Drosophila* embryonic SG as a model. This single-layered epithelial tube is formed through
98 highly stereotyped morphogenetic processes (Chung et al., 2014), making it an excellent system
99 for elucidating the molecular mechanisms underlying aECM composition and modification. SG
100 cells are specified on the ventral surface of the embryo at stage 10. Once specified, SG cells do
101 not undergo cell division or cell death because SG-upregulated transcription factors
102 downregulate the expression of key cell cycle genes and proapoptotic genes (Myat & Andrew,
103 2000a; Chandrasekaran & Beckendorf, 2003; Fox et al., 2013; Matthew et al., 2024), and thus
104 the entire morphogenetic process is driven by cell shape change, cell rearrangement, and
105 collective cell migration (Myat & Andrew, 2000b; Bradley & Andrew, 2001; Bradley et al.,
106 2003; Chung & Andrew, 2014; Chung et al., 2017). At stage 11, SG cells invaginate to form a
107 three-dimensional tubular structure, which then elongates and migrates toward its final position
108 during stages 12-13. The SG continues to migrate and the lumen expands significantly by apical
109 secretion during stages 14-16, forming the fully developed organ. Despite limited knowledge of
110 the composition of the aECM in the SG, previous work has demonstrated the critical role of
111 ADAMTS-A, a secreted metalloprotease, in releasing cells from the aECM to facilitate SG
112 migration and normal lumen shape (Ismat et al., 2013). Our previous work has also shown that
113 cell-aECM adhesion via the apical surface protein Cad99C influences cell rearrangement during
114 SG elongation (Chung & Andrew, 2014).

115 Here, we identify Papss as being essential for aECM organization and lumen expansion
116 of the *Drosophila* embryonic SG. Loss of *Papss* results in a disorganized apical membrane and a
117 condensed aECM, which is associated with disrupted Golgi structures and intracellular
118 trafficking. *Papss* mutants also show defects in the basal ECM and occasional SG cell death,
119 leading to invasion of hemocytes into SG epithelia that engulf dying cells. Expressing the wild-
120 type (WT) Papss in the SG rescues all phenotypes, but not the enzyme-dead form. We identify
121 two ZP proteins, Pio and Dpy, as key components of the SG aECM. In the SG lumen, these ZP
122 domain proteins form a filamentous scaffold that is significantly affected by the loss of *Papss*,

with Pio eventually being lost from the aECM and the Dpy-positive aECM structure condensing and dissociating from the apical membrane. Mutations in *pio* or *dpy*, or in *Notopleural* (*Np*), which encodes a matriptase that cleaves Pio to form the luminal pool of Pio, exhibit bulging and constriction of the SG lumen. Notably, mutations in *pio* result in the loss of luminal Dpy signals in the SG. These data indicate that the Dpy-containing filamentous structure of the aECM is crucial for maintaining luminal diameter and that the luminal pool of Pio is essential for organizing this structure during SG morphogenesis.

130 **Results**

131 **Papss is required for SG lumen expansion**

132 To identify key enzymes that affect SG morphology by modifying aECM components, we
133 examined the effects of the loss of ~20 enzymes that are highly expressed in the SG and are
134 likely to function in the secretory pathway (Fox et al., 2013). Deficiency lines deleting each
135 enzyme were immunostained with the apical membrane marker Crumbs (Crb) or Stranded at
136 Second (SAS) to assess SG lumen shape. Among the twelve lines showing defects (Table 1), a
137 deficiency line deleting *PAPS synthetase* (*Papss*) and 18 other genes had a very thin SG lumen
138 with irregular apical protrusions (Figure 1A). Papss catalyzes the synthesis of 3'-
139 phosphoadenosine-5'-phosphosulfate (PAPS), the sulfate donor compound in all sulfotransferase
140 reactions (Venkatachalam, 2003). Consistent with a previous report (Jullien et al., 1997), our
141 fluorescence in situ hybridization confirmed that *Papss* transcripts are highly expressed in the
142 SG throughout morphogenesis (Figure 1B), suggesting a high demand for sulfation in this organ.

143 To test the role of *Papss* and confirm the phenotype, we used a *Papss* EMS mutant line
144 (*Papss*^{2}; Zhu et al., 2005). The Papss protein contains two critical protein domains, the ATP
145 sulfurylase domain, which adds sulfate to an AMP group of ATP to form adenosine 5'-
146 phosphosulfate (APS), and the APS kinase domain, which phosphorylates APS to form PAPS
147 (Venkatachalam et al., 1998; Mueller & Shafqat, 2013). Sanger sequencing of this mutant
148 identified a point mutation (G->A) that introduces a premature stop codon (Trp271->stop; amino
149 acid number is for the Papss-PA isoform) located near the N-terminus of the ATP sulfurylase
150 domain, resulting in a truncated protein in which most of the domain is not translated (Figure 1-
151 figure supplement S1A-B). Since both protein domains are essential for the enzyme function of
152 Papss, we conclude that this mutant line is potentially null or a strong hypomorphic allele. *Papss*
153 homozygous mutants and transheterozygotes for *Papss* mutant over a deficiency were embryonic
154 lethal. To test the role of Papss in sulfation in the SG, we checked for the presence of sulfated
155 tyrosine using a sulfotyrosine antibody in WT and *Papss* mutant embryos. In WT, we observed
156 strong sulfotyrosine signals both in the apical membrane and as puncta in the cytoplasm of SG
157 cells (Figure 1-figure supplement S2A). The cytoplasmic puncta colocalized with ManII-GFP
158 signals, a medial Golgi marker (Yang et al., 2021), suggesting that proteins undergoing tyrosine
159 sulfation in the Golgi are detected by the antibody (Figure 1-figure supplement S2C). In *Papss*

160 mutants, the cytoplasmic punctate signals were significantly reduced (Figure 1-figure
161 supplement 2B), suggesting that sulfation in the Golgi is decreased. The signals at the apical
162 membrane appeared similar or slightly reduced compared to WT, suggesting that sulfated
163 molecules, possibly by maternally provided Papss, were still targeted apically, although it is not
164 clear whether they were properly targeted to their original destination or mislocalized. Together
165 with a previous study using Alcian Blue staining showing the loss of sulfated biomolecules in the
166 *Papss* mutant SG (Zhu et al., 2005), these data suggest sulfation in the SG is dependent on Papss.

167 *Papss* homozygous mutant embryos often showed overall defective embryonic
168 morphology, such as defects in germ band retraction and head involution (39%; N=80/204;
169 Figure 1-figure supplement 3A-F). The heterozygous *Papss* mutant embryos produced by
170 crossing *Papss* mutants with WT flies appeared normal (Figure 1-figure supplement 3A-F). A
171 smaller percentage of transheterozygous embryos showed similar defects (10%; N=13/136), with
172 many late-stage embryos appearing normal (Figure 1-figure supplement 3C, E and F). We
173 conclude that transheterozygous embryos with more severe defects did not survive to late stages,
174 but we cannot rule out the possibility that a secondary mutation at another gene locus contributes
175 to the overall embryonic defects. Embryos with these morphological defects often showed
176 defects in SG invagination, forming a SG close to the surface of the embryo (Figure 1-figure
177 supplement 3D, G and H). We used the embryos that formed the SG in the normal position for
178 quantification and further analysis.

179 Using the adherens junction (AJ) marker E-cadherin (Ecad) signals, we analyzed SG
180 lumen phenotypes in *Papss* homozygous mutant embryos and transheterozygotes. During stages
181 14-16, the WT SG lumen expanded consistently throughout its length (Figure 1C). In contrast,
182 *Papss* mutant embryos exhibited irregularities in SG lumen expansion. At stage 14, when the
183 WT SG lumen expansion began, more than 40% of *Papss* mutant embryos had either a thinner
184 lumen (Figure 1D and I; 18%; N=7/38) or a slightly irregular lumen with bulges (Figure 1D and
185 I; 24%; N=9/38). At stage 16, about half of *Papss* homozygous or mutant embryos or
186 transheterozygotes over a deficiency showed an overall thin lumen with an irregular apical
187 surface (Figure 1D and I') and the other half had an irregularly expanded lumen with thin and
188 expanded regions along its length (Figure 1D and I'). Quantification of the SG lumen length and
189 diameter at stage 16 showed that whereas the lumen length was comparable between WT and

190 *Papss* mutant SGs (Figure 1J), the diameter was significantly decreased or irregular, with a high
191 degree of variation in *Papss* mutant SGs (Figure 1K and K'). Quantification of the SG lumen
192 area at stage 16 revealed that *Papss* mutants SGs exhibiting the thin lumen phenotype had a
193 smaller lumen size compared to WT. Together, these data suggest a role for Papss in SG lumen
194 expansion primarily by expanding the lumen diameter (Figure 1L).

195 To determine whether the SG lumen expansion defects are due to the loss of *Papss*, we
196 performed a rescue experiment by overexpressing Papss in the SG using the SG-specific driver
197 *sage-Gal4* (Chung et al., 2009) in the *Papss* mutant background. *Papss* produces multiple
198 isoforms, including Papss-PA/B/C/G (629 aa), Papss-PD (657 aa), and Papss-PE/F/H (630 aa),
199 which differ only slightly in the N-terminus (Flybase; www.flybase.org). Using three additional
200 probes that detect different subsets of splice forms, we performed fluorescent in situ
201 hybridization and found that all probes detected signals in the SG at varying levels (Figure 1-
202 figure supplement 4A and B). We generated UAS lines for Papss-PD and Papss-PE and found
203 that overexpression of either isoform in the SG of WT embryos resulted in a normally expanded
204 SG lumen (data for Papss-PE overexpression are shown in Figure 1F and I'). Given the high
205 levels of *Papss* mRNA in the WT SG, the Papss protein is likely abundant in the SG, which may
206 explain why further overexpression of Papss does not lead to any additional effects. Since our
207 initial analysis showed identical rescue features in the SG for the generated UAS lines, we used
208 the UAS-Papss-PD and UAS-Papss-PE lines interchangeably for further experiments (hereafter,
209 when overexpressed, Papss-PD and Papss-PE will be referred to as Papss). When Papss was
210 overexpressed in the SG of *Papss* mutant embryos, only a small fraction (4%; N=1/26) showed a
211 thin lumen phenotype along the entire length of the SG (Figure 1G and I'). The majority of
212 embryos (73%) showed either a normal, fully expanded lumen along the entire length of the SG,
213 with occasional slight irregularities at the apical membrane (42%; N=11/26), or a irregularly
214 expanded lumen, where some parts of the SG lumen were expanded and others were thin (31%;
215 N=8/26) (Figure 1G and I'). SGs with normally expanded lumens had luminal geometry
216 comparable to that of WT embryos (Figure 1J-L). Interestingly, some of the embryos had an
217 over-expanded SG lumen, often with a non-uniform diameter (24%; N=6/24; Figure 1G and I').
218 To test whether the enzyme activity of Papss is required for its role in SG lumen expansion, we
219 also generated UAS lines with mutations in the critical residues of the ATP sulfurylase (F593P)
220 and APS kinase (K193A) domains using the Papss-PD isoform (See Materials and Methods for

221 details; amino acid number is for Papss-PD). Overexpressing a mutant version of Papss
222 containing both of these mutations in the SG did not rescue the SG phenotypes as WT Papss did,
223 but it showed the same range of defects as *Papss* mutants (Figure 1H, I' and J-L). These data
224 suggest that the sulfation activity of Papss is required for SG lumen expansion. Overall, although
225 a range of phenotypes was present, the thin SG lumen phenotype was almost completely rescued
226 by SG-specific expression of WT Papss, but not the enzyme-dead form.

227

228 **Loss of *Papss* disrupts the apical domain and aECM organization**

229 To investigate the cellular basis of the thin SG lumen phenotype in *Papss* mutants, we examined
230 the localization of key apical membrane proteins and junctional markers. In WT SGs, the apical
231 polarity protein Crb localized to the subapical region (SAR) between the apical surface (free
232 apical area) and the AJs, and we observed clear Crb signals along the apical cell boundary of
233 each SG cell (Figure 2A and B). In contrast, the Crb signals in *Papss* mutants appeared less
234 prominently localized to the SAR in SG cells (Figure 2C). We measured the Crb signal intensity
235 in the SAR and the apical-medial region of SG cells. The ratio of the Crb signal intensity at SAR
236 to apical-medial intensity was significantly lower in *Papss* mutants than in WT (Figure 2D),
237 indicating disorganization of the apical domain. The AJ marker Ecad and the septate junction
238 (SJ) marker Discs large (Dlg) showed no apparent disruption in localization compared to WT
239 (Figure 2-figure supplement 1A-E). These data suggest that loss of *Papss* primarily affects the
240 apical membrane in the SG, while leaving the junctional regions intact.

241 Next, we investigated the organization of the aECM, using wheat germ agglutinin (WGA),
242 which marks several glycan modifications including O-linked β-N-acetylglucosamine (O-
243 GlcNAc). WGA has been shown to label the apical membrane and luminal structure in the
244 *Drosophila* embryonic trachea (Tonning et al., 2005; Chung et al., 2009). Similarly, we observed
245 relatively weak WGA signals in the apical membrane and the lumen of WT SGs (Figure 2E; n=25
246 SGs). Notably, the luminal signals showed multiple thin filamentous organizations traversing the
247 lumen (Figure 2E), suggesting heterogeneity of the luminal structure. In *Papss* mutants, WGA
248 signals were increased in both the lumen and apical membrane, with the apical membrane signals
249 appearing more diffuse (Figure 2F; n=28 SGs). Interestingly, the luminal WGA signals in *Papss*

250 mutants accumulated strongly on one side along the entire length of the lumen, whereas the thin
251 filamentous WGA signals in WT SGs appeared to show no bias and were mostly centered in the
252 lumen. In regions with a thin SG lumen, WGA was present in a highly condensed rod-like
253 structure; in expanded regions, WGA signals showed either a similar condensed rod-like structure
254 favoring one side of the SG lumen or a slightly condensed filamentous structure often broadly
255 associated with the apical membrane (Figure 2F). Transmission electron microscopy (TEM)
256 analysis also revealed highly condensed and more electron-dense luminal structures in the SG of
257 *Papss* mutants compared to WT (Figure 2H and I; original, raw TEM images of several WT and
258 *Papss* mutant samples are shown in Figure 2-figure supplement 2A and B). SG-specific
259 overexpression of Papss in the *Papss* mutant background resulted in a partial rescue; the luminal
260 WGA structures were less condensed than *Papss* mutants, but they were not as thin as those in WT
261 SGs (Figure 2G). Taken together, these data suggest a role for Papss in organizing the SG aECM
262 with loss of *Papss* resulting in a tightly packed or condensed aECM that is loosely associated with
263 the apical membrane.

264

265 **Loss of *Papss* disrupts Golgi organization and mislocalizes intracellular trafficking**
266 **markers**

267 In addition to the apical membrane and luminal signals, we detected WGA signals around the
268 nucleus, consistent with WGA binding to glycoproteins on the nuclear envelope (Rutherford et al.,
269 1997), and in several large, punctate cytoplasmic structures in WT SG cells (Figure 3A and E).
270 The cytoplasmic WGA puncta colocalized with the medial-Golgi marker ManII-GFP, suggesting
271 that WGA binds glycoproteins in the Golgi (Figure 3J and L). The number and intensity of the
272 punctate WGA signals were significantly reduced in *Papss* mutants (Figure 3B, F, I and I').
273 Overexpression of WT Papss, but not the mutant form of Papss, in the SG restored the number of
274 WGA cytoplasmic puncta (Figure 3C, D, G, H, I and I'). The intensity of the WGA signals was
275 not restored in either case (Figure 3I').

276 Interestingly, we observed highly dispersed ManII-GFP signals in *Papss* mutants SGs
277 (Figure 3K and L'), suggesting that Golgi structures may be disrupted upon *Papss* loss. To examine
278 the Golgi structures in more detail, we performed TEM analysis in WT and *Papss* mutant SG cells.

279 In contrast to the mammalian Golgi, the *Drosophila* Golgi lacks the characteristic ribbon-like
280 structure and is composed of a series of individual cisternae arranged in a random, disordered
281 fashion (Kondylis & Rabouille, 2009). While the Golgi in WT SG cells showed randomly arranged
282 cisternae, the Golgi in *Papss* mutants showed abnormal arrangement, either stacked or
283 compressed, with small electron-dense puncta along these structures (Figure 3M and N),
284 suggesting a functional defect and possible protein aggregation. Other organelles, such as the
285 endoplasmic reticulum (ER), appeared relatively normal. SG-specific expression of GFP-KDEL,
286 GFP fused to the ER retention motif KDEL, or immunostaining for prolyl-4-hydroxylase-alpha
287 SG1, an ER-resident enzyme (Abrams et al., 2006), showed no significant differences between
288 WT and *Papss* mutant SGs (Figure 3-figure supplement 1 A-D). TEM analysis also revealed
289 similar ER structures in WT and *Papss* mutant SG cells (Figure 3-figure supplement 1E and F).
290 These data suggest that loss of *Papss* disrupts the Golgi, but not the ER.

291 To determine whether the phenotypes observed in *Papss* mutants are due to defects in
292 Golgi structure and function, we examined the morphology of the SG in null mutants of two key
293 Golgi components, GM130 and Grasp65 (Zhou et al., 2014). Both mutants were homozygous-
294 viable. Although the GM130 null allele ($GM130^{\Delta 23}$) was extremely weak and difficult to grow, the
295 embryos we managed to collect appeared normal, and the SG exhibited only mild irregularity
296 (Figure 3-figure supplement 2A; n=5/5). It is possible that only relatively normal embryos survived
297 until late stages of embryogenesis. However, *Grasp65* null mutants ($Grasp65^{102}$) exhibited a
298 highly irregular SG lumen with condensed luminal WGA signals (Figure 3-figure supplement 2B
299 and C; n=10/10). These data suggest that disrupted Golgi structures in *Papss* mutants may
300 contribute to the SG defects.

301 The aberrant Golgi structures observed in *Papss* mutants prompted us to investigate the
302 impact on intracellular trafficking components. We examined the localization of Rab11, a marker
303 for recycling endosomes, Rab7, a marker for late endosomes, and Sec15, an exocyst marker. As
304 previously shown (Chung & Andrew, 2014; Le & Chung, 2021), Rab11 and Sec15 were enriched
305 along the apical domain of WT SG cells (Figure 3O and Q). In *Papss* mutants SGs, we observed
306 an increase in apical Rab11 signal intensity, with some signals mislocalized to the basolateral
307 region (Figure 3P and S). In contrast, Sec15 signals were significantly reduced at the apical
308 membrane (Figure 3R and T). Unlike Rab11 or Sec15, Rab7 localized in large punctate structures

309 in the cytoplasm of WT SG cells (Figure 3-figure supplement 3A). In *Papss* mutants, the number
310 of Rab7 puncta was significantly reduced, although the intensity of Rab7 puncta was not
311 significantly different from WT (Figure 3-figure supplement 3B-D). TEM analysis revealed a
312 number of electron-dense vesicles in the apical domain of SG cells in WT (Figure 3U). In contrast,
313 *Papss* mutant SGs showed fewer electron-dense vesicles, but instead we observed several larger,
314 empty vesicle-like structures (Figure 3V and W). Collectively, these data suggest that defective
315 sulfation affects Golgi structures and multiple routes of intracellular trafficking.

316

317 **Loss of *Papss* results in abnormal cell death and disruption of the basal ECM**

318 In *Papss* mutant embryos, we often observed one or more acellular regions within the SG
319 epithelium during late embryogenesis that lacked any markers for nuclei, cell membranes, or
320 junctions. To test whether these acellular regions were caused by cell death, we stained embryos
321 with an antibody against *Drosophila* cleaved death caspase-1 (DCP-1; Sarkissian et al., 2014).
322 Indeed, DCP-1 signals were often found within the acellular spaces (Figure 4A and B),
323 suggesting that loss of *Papss* leads to abnormal cell death in the SG. TEM analysis also captured
324 a dying cell in the *Papss* mutant SG supporting the occurrence of cell death (Figure 4C). We
325 found that *Papss* mutant SGs have a significantly higher number of these acellular spaces
326 compared to WT SGs (Figure 4D). Quantifying the number of SG cells at stage 16 revealed that
327 *Papss* homozygous embryos and transheterozygotes have significantly fewer cells than WT
328 (Figure 4E). Overexpression of WT Papss, but not the mutant form of Papss, in the *Papss* mutant
329 background decreased the number of acellular regions within the SG (Figure 4D) and restored
330 the number of SG cells (Figure 4E). This suggests that loss of sulfation leads to conditions that
331 hinder SG cell survival. Blocking apoptosis in the *Papss* mutant SG by overexpressing the
332 baculoviral protein p35, a caspase inhibitor of apoptosis, also restored the SG cell number
333 (Figure 4E), suggesting that apoptosis is a key mechanism underlying SG cell loss in *Papss*
334 mutants. Importantly, the SGs in these embryos still showed thin (25%; N=2/8) or irregularly
335 expanded (75%; N=6/8) lumens, suggesting that SG lumen expansion defects in *Papss* mutants
336 are independent of abnormal cell death.

337 Using srpHemo3x-mCh (Gyoergy et al., 2018), we labeled hemocytes, which are
338 analogous in function to macrophages in vertebrates. Hemocyte signals were often present in the
339 acellular regions of the SG in *Papss* mutants, suggesting that hemocytes may aid in apoptotic cell
340 clearance from the SG epithelium (Figure 4F and G). In normal epithelia, the basal ECM acts as
341 a physical barrier, preventing hemocytes from migrating into the epithelial layer. To examine the
342 integrity of the basal ECM in *Papss* we used an antibody against Nidogen (Ndg), a glycoprotein
343 with important linker functions in the basement membrane (Wolfstetter & Holz, 2012). Ndg-
344 positive basal ECM was detected in a regular, thin layer around WT SGs at stage 16 (Figure 4H).
345 However, in *Papss* mutants, Ndg signals were irregular and often disconnected, and hemocytes
346 invaded SG cells through the gaps in the Ndg-positive basal ECM (Figure 4I). Overall, our data
347 suggest that loss of *Papss* leads to aberrant cell death in the SG and disrupts both the apical and
348 basal ECM of the SG.

349

350 **The ZP domain proteins Pio and Dpy of the SG aECM are affected by the loss of *Papss***

351 To better understand how aECM composition and organization are affected by *Papss* loss, we set
352 out to identify SG aECM components. Since chitin, a major aECM component in many *Drosophila*
353 tissues, is absent from the SG lumen (Figure 5A), we focused on ZP domain proteins. Of the 18
354 ZP domain proteins in *Drosophila*, at least six are expressed in the embryonic SG, including *pio*,
355 *dpy*, *quasimodo* (*qsm*), *cypher* (*cyr*), *dusky* (*dy*), and *CG17111* (Tomancak et al., 2002; Jazwinska
356 & Affolter, 2004; Weiszmann et al., 2009). We assessed the localization of Pio and Dpy, key
357 aECM components critical for *Drosophila* tracheal morphogenesis (Jazwinska et al., 2003; Drees
358 et al., 2023), and Qsm, which plays a critical role in remodeling Dpy in the aECM during
359 *Drosophila* flight muscle development (Chu & Hayashi, 2021).

360 To test Pio localization in the SG, we used a transgenic line expressing an mCherry-Pio
361 (mCh-Pio) fusion protein with the N-terminal mCh tag (Drees et al., 2023; Figure 5B), as well as
362 a Pio antibody generated with the peptide corresponding to the sequence within the ZP domain of
363 Pio, between the ZP-N and ZP-C domains (Jazwinska et al., 2003; Figure 5B). mCh-Pio signals
364 were observed in cytoplasmic puncta, at the apical membrane, and in the SG lumen. These signals,
365 especially the luminal signals, became stronger at stages 15-16 (Figure 5C), suggesting that Pio is

366 transported apically and secreted into the SG lumen. Pio antibody signals showed distinct
367 localization, predominantly in the SG lumen and at the apical membrane (Figure 5E and F). At
368 stages 11 and 12, the Pio antibody revealed low levels of cytoplasmic punctate signals along with
369 strong luminal signals, but from stage 13, Pio signals were predominantly localized to the SG
370 lumen (Figure 5E and F; Figure 5-figure supplement 1A). Interestingly, compared to the diffuse
371 luminal mCh-Pio signals (Figure 5C), Pio antibody signals in the SG lumen were heterogeneous
372 with filamentous structures (Figure 5E-6F''), resembling luminal WGA signals. Pio antibody
373 signals were absent at all stages in the *pio* null mutant, in which the entire ZP domain is deleted
374 (Drees et al., 2023; Figure 5-figure supplement 1B and C), confirming antibody specificity. The
375 Pio protein is known to be cleaved, at one cleavage site after the ZP domain, possibly by a furin
376 protease, and at another cleavage site within the ZP domain by the matriptase Notopleural (Np)
377 (Drees et al., 2019; Drees et al., 2023; Figure 5B). The latter cleavage site falls within the peptide
378 sequence used to generate the Pio antibody (Figure 5B). A possible explanation for the different
379 signals between mCh-Pio and Pio antibody signals is that the Pio antibody preferentially
380 recognizes the C-terminal ZP domain fragment after furin and Np cleavage, whereas diffuse,
381 luminal mCh-Pio signals are either the secreted Pio protein cleaved only by furin or the N-terminal
382 fragment after Np cleavage.

383 Dpy-YFP signals from the Dpy-YFP knock-in line (Lye et al., 2014; YFP insertion into the
384 *dpy* locus near the middle of the protein) showed heterogeneous, filamentous structures in the SG
385 lumen throughout SG morphogenesis (Figure 5-figure supplement 2A) that colocalized with Pio
386 antibody and WGA signals (Figure 5E-F"; Figure 5-figure supplement 2C). It should be noted that
387 because homozygous Dpy-YFP embryos showed a bulging and constricted SG lumen phenotype
388 with highly condensed Dpy-YFP signals throughout the lumen (Figure 5-figure supplement 2B),
389 we used embryos with one copy of the transgene to analyze Dpy localization. Qsm localization
390 was analyzed using the mCh-Qsm knock-in line, in which mCh is inserted into the *qsm* locus a
391 few amino acids downstream of the N-terminal end of the protein (Chu & Hayashi, 2021). Unlike
392 Pio and Dpy, mCh-Qsm signals were not detected in the SG lumen. Instead, they showed a
393 dynamic intracellular localization ranging from cytoplasmic signals with apical membrane
394 enrichment (stages 11-14) and apical vesicular signals (stages 14-15) to prominent signals at the
395 apical membrane and SJs (stage 16) (Figure 5-figure supplement 3A). These data suggest that Qsm
396 is not a component of the SG aECM. However, it is possible that the mCh-Qsm signals only detect

397 the cleaved N-terminal fragment of Qsm, while the C-terminal fragment may localize to a different
398 subcellular location. Taken together, our data suggest that Pio and Dpy form filamentous aECM
399 structures in the SG.

400 We next examined Pio, mCh-Pio, Dpy-YFP, and mCh-Qsm signals in *Papss* mutant SGs
401 at stages 14 and 16. At stage 14, Pio antibody and Dpy-YFP signals appeared condensed and
402 enriched within the SG lumen, with reduced association with the apical membrane compared to
403 WT (Figure 5G and G'). Interestingly, Pio antibody signals were barely detectable in the SG
404 lumen at stage 16 (Figure 5H-H'''), likely due to either protein degradation or epitope masking
405 caused by aECM condensation and protein misfolding. In contrast, Dpy-YFP signals remained in
406 the lumen at all stages and were condensed and localized to one side of the lumen at stage 16
407 (Figure 5H-H'''), similar to WGA signals (Figure 2E). mCh-Pio signals were depleted from the
408 expanded region of the lumen but weak signals colocalized with condensed Dpy-YFP signals
409 (Figure 5D). We did not observe any significant differences in the localization or intensity of
410 mCh-Qsm signals in *Papss* mutants (Figure 5-figure supplement 3B and C). These data suggest
411 that the luminal pool of Pio and Dpy, which form filamentous structure, is significantly affected
412 by the loss of *Papss*, resulting in the loss of Pio and the condensation and dissociation of the
413 Dpy-containing aECM structure from the apical membrane.

414

415 **ZP domain matrix is required for uniform SG lumen diameter**

416 We next investigated the role of Pio and Dpy in SG morphogenesis by analyzing SG lumen
417 morphology in *pio* and *dpy* mutants. Immunostaining with Ecad revealed that *pio* null mutants
418 formed relatively normal SGs up to stage 15, but stage 16 SGs showed dramatically abnormal
419 luminal morphology characterized by multiple constrictions, with a slight expansion of the lumen
420 between constrictions (Figure 6A, B and F; Figure 6-figure supplement 1B). The constricted
421 regions were severely narrowed to the point of almost no luminal space, and some luminal regions
422 also showed a flat protrusion on one side of the SG lumen (Figure 6C). Notably, these abnormal
423 luminal shapes were associated with a progressive loss of luminal WGA and Dpy-YFP signals
424 (Figure 6B, D). In *pio* mutants, WGA signals were comparable to WT at stages 13 and 14 (Figure
425 6-figure supplement 1A-B), but appeared slightly reduced and diffuse in the SG lumen at late stage

426 14, and this reduction became more pronounced at stage 15 (Figure 6A and B). Dpy-YFP signals
427 were more severely affected in *pio* mutants. Unlike the strong, filamentous luminal signals in the
428 control (Figure 5-figure supplement 1A), Dpy-YFP signals were reduced and diffuse in the SG
429 lumen and were detected in the cytoplasm of *pio* mutant SG cells from stage 12 to stage 14, with
430 a conspicuous absence in the lumen at stage 15 (Figure 6-figure supplement 1C). By stage 16, both
431 WGA and Dpy-YFP signals were completely absent from the lumen in *pio* mutants, whereas the
432 signals were still present at the apical membrane and in the cytoplasm (Figure 6B and D). We
433 conclude that WGA primarily detects Dpy in the SG lumen and that Pio is required for Dpy
434 secretion to the SG lumen.

435 To test a role for Pio cleavage and localization in shaping the SG lumen, we analyzed embryos
436 mutant for the matriptase Np, which cleaves Pio. In *Np* mutants, Pio and WGA signals were
437 observed in both the apical membrane and lumen up to stage 14, similar to WT embryos (Figure
438 6E). However, at stage 16, Pio signals were observed closely associated with the apical membrane,
439 with no luminal Pio signals present (Figure 6E), suggesting that Np is required for this luminal
440 pool of Pio. Importantly, *Np* mutants exhibited the same bulging and constricting SG luminal
441 phenotype at stage 16 as *pio* mutants (Figure 6E and F), indicating that the filamentous luminal
442 Pio structure plays a crucial role in maintaining a uniform SG diameter.

443 *dpy* mutants (dpy^{ov1}; a spontaneous mutant with a transposable element insertion into intron 11)
444 exhibited a more severe bulging and constriction phenotype in the SG lumen compared to *pio*
445 mutants. Until stage 14, SGs in *dpy* mutants often showed a curved shape, but otherwise had a
446 relatively normal morphology and uniform diameter (Figure 6-figure supplement 1D). At stages
447 15 and 16, SG lumen lost regularity and uniformity, often exhibiting multiple bulges and
448 constrictions. (Figure 6G and G'). In constricting regions, we observed condensed Pio and WGA
449 signals in the lumen, whereas in bulging regions, weak Pio and WGA signals were detected along
450 the apical boundaries (Figure 6G and G'). These data suggest a disrupted luminal scaffold that
451 correlates with the bulging and constricting luminal morphology.

452 To further investigate the role of Np in cleaving Pio to organize the aECM during SG
453 morphogenesis, we overexpressed WT (Np^{WT}) and mutant (Np^{mut}) forms of Np using the UAS-
454 Np-Strep and UAS-Np.S990A-GFP lines (Drees et al., 2019). It should be noted that the
455 endogenous Np remains when either form of Np is overexpressed in the SG. Overexpression of

456 Np^{WT} increased the intensity of luminal mCh-Pio signals (Figure 6H), whereas overexpression of
457 Np^{mut} resulted in the absence of the mCh-Pio signals in the lumen but strong mCh-Pio signals close
458 to the apical membrane and in the cytoplasmic puncta (Figure 6I), supporting the role of Np in
459 cleaving Pio to generate the luminal pool of Pio. In Np^{WT}-overexpressing SGs, the overall intensity
460 of Pio and Dpy-YFP signals also appeared increased at both the apical membrane and in the lumen
461 compared to WT (Figure 6H). These embryos did not show obvious changes in the SG
462 morphology. In Np^{mut}-overexpressing SGs, Pio signals appeared to be increased at the apical
463 membrane, and various levels of filamentous luminal signals were detected (Figure 6I-I'').
464 Importantly, the regions of the lumen lacking luminal Pio signals was always slightly expanded
465 compared to the region with filamentous luminal Pio signals, supporting the idea that the luminal
466 Pio pool is important for a uniform lumen diameter (Figure 6I' and I''; n=11/13). Dpy-YFP signals
467 could not be analyzed properly with Np^{mut} overexpression because of the GFP tag in the Np^{mut}
468 transgene. However, we detected two distinct pools of fluorescent signals in the GFP channel. The
469 first pool was cytoplasmic punctate signals that colocalized with mCh-Pio, which we confirmed
470 are Np^{mut}-GFP signals in a separate staining, and the second pool was thin filamentous luminal
471 signals that overlapped with Pio antibody signals, which we suspect are Dpy-YFP signals (Figure
472 6I). These data suggest that overexpressed Np^{mut} failed to cleave mCh-Pio and Pio, leading to their
473 accumulation at and near the apical membrane, but the endogenous Np still cleaved some pool,
474 resulting in low levels of filamentous luminal Pio structures. Taken together, our data suggest that
475 Dpy and Pio form a luminal scaffold necessary for a uniform SG tube diameter and that Pio
476 cleavage by Np is essential for forming this scaffold.

477

478 **Discussion**

479 Our study highlights the critical role of Papss, a key enzyme that produces the universal sulfate
480 donor PAPS, in aECM organization and lumen expansion in the *Drosophila* embryonic SG.
481 *Papss* mutants show defective SG lumen expansion, accompanied by disruption of the apical
482 domain of SG cells and the aECM. The loss of *Papss* leads to defects in Golgi and intracellular
483 trafficking, abnormal cell death in the SG, and defective basal ECM, emphasizing the importance
484 of sulfation in multiple developmental processes. We also identify the ZP domain proteins Dpy
485 and Pio as key components of the SG aECM, where Dpy is a scaffolding aECM structure that
486 provides mechanical support and Pio is required for proper organization of this structure.

487

488 **Sulfation is critical for aECM organization and SG lumen expansion**

489 During *Drosophila* SG morphogenesis, secreted cargos are modified in the Golgi, secreted
490 apically, and deposited in the lumen to form the aECM meshwork. Our data show that sulfation
491 is essential for the proper organization of the aECM and the formation of a normal SG luminal
492 shape. Consistent with a high demand for sulfation in the SG, transcripts for *Papss* and several
493 other key enzymes involved in sulfation reactions are also upregulated in the SG, including
494 *slalom* (*sll*), which encodes the *Drosophila* PAPS transporter (Kamiyama et al., 2003; Luders et
495 al., 2003), and *pipe* (*pip*) and *tyrosylprotein sulfotransferase* (*Tpst*), which encode
496 sulfotransferases. Notably, Alcian Blue-stained materials are absent from the SG in *Papss*, *sll*, or
497 *pip* mutants (Zhu et al., 2005), suggesting that sulfation in the SG depends entirely on these
498 enzymes. Our data show that the irregularly expanded SG lumen phenotype in *Papss* mutants is
499 associated with the condensed aECM structures and reduced association of the aECM with the
500 apical membrane (Figures 1 and 2). Inappropriate charge balance due to defective sulfation of
501 proteoglycans and glycoproteins, as well as protein misfolding or failure to bind to appropriate
502 partners, may contribute to aggregation of aECM components and condensation of the aECM
503 structure. The ubiquitously expressed human *Papss1* gene shows upregulation in several
504 glandular organs and the salivary duct (Uhlen et al., 2005; Karlsson et al., 2021), suggesting a
505 potentially conserved role for this enzyme in modifying secreted molecules and modifying
506 aECM in these organs.

507 The defects in SG lumen expansion in *Papss* mutants are linked to defects in intracellular
508 trafficking, characterized by aberrant Golgi structures and mislocalized or reduced levels of
509 several vesicle markers (Figure 3). This suggests that the loss of *Papss* has a broader impact on
510 the intracellular trafficking system, beyond the sulfation of specific substrate molecules. Mutants
511 of the key Golgi component Grasp65 show a mildly irregular SG lumen (Figure 3-figure
512 supplement 3), supporting the important role of the Golgi in establishing proper lumen
513 dimensions during organ formation. Consistent with the idea that the secretory pathway plays a
514 key role in trafficking aECM components to the lumen, several mutants in intracellular
515 trafficking genes, such as *CrebA*, *Sec61β*, and *Sar1*, which encode a major transcription factor
516 that boosts secretory capacity, a Sec61 translocon component, and a COPII vesicle formation
517 component, respectively, have been shown to have a slightly thinner SG lumen (Fox et al., 2013;
518 Fox & Andrew, 2015). However, the defects in *Papss* mutants differ from those in general
519 secretion mutants. While the latter exhibit a uniformly thin lumen, altered localization of several
520 subcellular organelles including mitochondria and the ER, and reduced Golgi signals (Fox &
521 Andrew, 2015), *Papss* mutants show an irregularly expanded lumen and primarily affect the
522 Golgi, while other organelles remain largely intact (Figure 3 and Figure 3-figure supplement 1).
523 Some of the abnormally modified targets appear to be aggregated in the defective Golgi in *Papss*
524 mutants, but many are still transported apically and secreted into the lumen, resulting in a highly
525 condensed luminal aggregate.

526

527 **The role of ZP domain proteins in non-chitinous aECM in the SG**

528 We are beginning to understand the structural components and biological functions of the non-
529 chitinous aECM during tubular organ formation. For example, in the non-chitinous aECM of the
530 *C. elegans* vulva and excretory duct, distinct aECM components, including zona pellucida (ZP)
531 domain proteins, chondroitin proteoglycans, and glycoproteins, work together to form the lumens
532 of these tubular organs (Gill et al., 2016; Cohen, Sparacio, et al., 2020). Our work reveals that
533 two ZP proteins, Dpy and Pio, play essential roles in organizing the aECM in the *Drosophila* SG,
534 highlighting the important role of ZP proteins in forming the non-chitinous luminal matrix
535 during tubular organ formation. Dpy, a gigantic protein (>2 MDa) with hundreds of epidermal
536 growth factor (EGF) repeats interspersed with a Dpy module, forms long filamentous structures

537 (Wilkin et al., 2000). With these filamentous structures, Dpy plays an essential role in the
538 organization and attachment of apical structures in several tissues, including the thoracic cuticle
539 (Wilkin et al., 2000), embryonic trachea (Jazwinska et al., 2003), pupal wings (Bokel et al.,
540 2005), genitalia (Smith et al., 2020), and muscle tendon cells (Chu & Hayashi, 2021). In the SG,
541 aberrantly formed or lost luminal Dpy structures correlate with abnormal luminal morphology
542 (Figures 5, 6 and Figure 5-figure supplement 2). We propose that the Dpy filamentous structure
543 provides mechanical support in the SG aECM and that proper organization of these structures is
544 critical for the formation of a uniform tube diameter. WGA signals always colocalize with Dpy-
545 YFP signals in WT and *Papss* mutants, and both signals are absent from the lumen in *pio*
546 mutants. WGA may primarily detect Dpy in the SG lumen by binding sugar residues that are
547 attached to numerous EGF modules of the Dpy protein. A caveat to the analysis of Dpy using the
548 Dpy-YFP line is that it is a non-functional fusion protein. An antibody against Dpy or a new
549 functional fusion protein will be required to confirm Dpy localization. Even with this caveat, our
550 data with the Pio antibody suggest that Dpy forms the filamentous luminal structure with Pio. Pio
551 is required to secrete and maintain Dpy in the lumen of the SG (Figure 6). This is consistent with
552 a role for Pio in Dpy secretion in the *Drosophila* trachea (Drees et al., 2023) and suggests a
553 conserved role for Pio in multiple tissues. Since the ZP domains of Pio and Dpy have been
554 shown to bind directly to each other in vitro (Drees et al., 2023), it is likely that the binding of
555 Pio and Dpy is required for the formation of filamentous luminal structures. This binding may
556 require cleavage of Pio by the matriptase Np, which generates the filamentous luminal pool of
557 Pio (C-terminal ZP fragment of Pio). *pio* and *Np* mutants show similar bulging and constricting
558 SG lumen morphology (Figure 6), suggesting that the generation of the C-terminal ZP fragment
559 of Pio by Np is critical for the formation of the filamentous luminal structure with Dpy.

560 Papss plays an essential role in the formation of the filamentous Dpy/Pio structure
561 (Figure 5). It will be important to learn if the defects of the Pio-Dpy matrix in *Papss* mutants is a
562 direct consequence of the loss of sulfation on these proteins or if it's an indirect outcome. The ZP
563 domain can mediate homomeric or heteromeric polymerization into filaments, and its structure is
564 stabilized by disulfide bonds formed between conserved Cys residues responsible for the
565 polymerization of ZP modules (Jovine et al., 2002). Defective disulfide bond formation due to
566 defective sulfation may destabilize Pio-Dpy interactions. Additionally, hundreds of EGF
567 modules in the Dpy protein are highly susceptible to O-glycosylation. Sulfation of the glycan

568 groups attached to Dpy may be critical for its ability to form a filamentous structure. In the
569 absence of sulfation, the glycan groups on Dpy may not properly interact with the surrounding
570 materials in the lumen, resulting in an aggregated and condensed structure. However, additional
571 key substrate(s) of Papss, such as mucins, may exist in the SG aECM that play a key role in
572 lumen expansion and shape. The striking enrichment of *Papss* expression in the SG compared to
573 other tubular organs, such as the trachea, implies that the key substrate(s) of Papss are likely
574 unique to or more highly enriched in the SG aECM than in the tracheal aECM.

575 It will be interesting to determine the role of other ZP proteins highly expressed in the SG.
576 Qsm, for example, has been found in the same intracellular vesicles as Dpy in *Drosophila* tendon
577 cells and has been shown to physically interact with Dpy through their ZP domains (Chu &
578 Hayashi, 2021). Qsm has been shown to remodel Dpy filaments that link tendon cells to the pupal
579 cuticle, increasing their tensile strength (Chu & Hayashi, 2021). In the SG, we find that Qsm is
580 mainly localized to cytoplasmic vesicles and AJ/SJ regions rather than being present in the SG
581 lumen like Pio and Dpy. It should be noted that like Pio, Qsm has a furin cleavage site near the
582 transmembrane domain and another putative protease cleavage site in the ZP domain. Since the
583 mCh-Qsm line contains the mCh insertion near the N-terminal end of the protein, the mCh-Qsm
584 signals are likely those of the cleaved N-terminal fragment after cleavage by these proteases and
585 will need to be confirmed using western blot. Further investigation will be needed to determine
586 the role of Qsm in junctional regions of SG cells. Also, the roles of other SG-upregulated ZP
587 domain proteins remain to be elucidated.

588 In conclusion, our analysis of the *Drosophila Papss* gene, a single ortholog of human
589 Papss1 and Papss2, reveals its multiple roles during SG development. We expect that these
590 findings will provide important insights into the function of these enzymes in normal
591 development and disease in humans. Our findings on the key role of two ZP proteins, Pio and
592 Dpy, as major components of the SG aECM also provide valuable information on the
593 organization of the non-chitinous aECM during organ formation.

594

595 **Materials and Methods**

596 **Fly stocks and genetics**

597 The fly stocks used in this study are listed in Table S2. All the crosses were performed at 25°C.

598

599 **Generation of transgenic lines**

600 UAS lines for the Papss-PD (657 aa) and Papss-PE/F/H (630 aa; hereafter referred to as Papss-
601 PE) isoforms were generated. Papss-PD and Papss-PE differ only slightly in the N-terminus.
602 Two UAS clones, UFO09742 (DGRC Stock 1643418;
603 https://dgrc.bio.indiana.edu//stock/1643418 ; RRID:DGRC_1643418) and UFO09743 (DGRC
604 Stock 1643419 ; https://dgrc.bio.indiana.edu//stock/1643419 ; RRID:DGRC_1643419), were
605 obtained from the *Drosophila* Genomics Resource Center. UFO09742 was generated from the
606 RE15281 cDNA clone encoding the open reading frame (ORF) for the Papss-PD isoform.
607 UFO09743 was generated using the RE03925 cDNA clone, which encodes the same ORF for the
608 Papss-PE isoform. Each clone contains a C-terminal Flag-HA tag. Purified DNA for the UAS
609 clones (500 ng/µl) was sent to GenetiVision (Houston, TX) for injection. GenetiVision
610 performed PhiC31-mediated insertions using the attP40 site.

611 UAS-Papss mutant lines for the APS kinase and ATP sulfurylase domains were generated
612 by site-directed mutagenesis using the UAS-Papss-PD construct (UAS-Papss-PD^{K193A}, UAS-
613 Papss-PD^{F593P}, and UAS-Papss-PD$^{K193A, F593P}$). K161 and F550 in human Papss (K193 and F593
614 residues of *Drosophila* Papss-PD*)* were identified as being critical for the catalytic efficiency of
615 the APS kinase and ATP sulfurylase domains, respectively (Zhang et al., 2022; Zhang et al.,
616 2023), and were mutated to alanine and proline, respectively. The UAS-Papss-PD construct was
617 amplified using the NEB Q5 master mix and the following primers.

618 **Primers used to make *UAS-Papss-PD^{K193A}***

619 Primer forward: 5'-CCGGGACGTGGCGGGTCTATACAAG-3'

620 Primer reverse: 5'-GTTTCGCACACATCCAG-3'

621 **Primers used to make *UAS-Papss-PD^{F593P}***

622 Primer forward: 5'-GATCCTGCCCCCGCGTGTTGCTG-3'

623 Primer reverse: 5'-TCCATGCTGTCTAGTC-3'

624 Following amplification, a kinase, ligase, and DpnI (KLD) reaction was performed and the
625 mutant construct was transformed into DH5α competent cells. To screen for colonies containing
626 a correct mutation, plasmid DNAs were isolated and the ORF of *Papss* was sequenced using the
627 following primers.

628 **Primers for sequencing the *Papss* ORF**

629 **Forward primer 1:** 5'-TGACCGAGCAAAAGCACCAT-3'

630 **Forward primer 2:** 5'-CGAGGTGGCCAAGTTGTTTG-3'

631 **Forward primer 3:** 5'-CCCGAGTTCTACTTTCAGCGT-3'

632 **Forward primer 4:** 5'-GCCGGTGCGAACTTCTACAT-3'

633 **Reverse primer:** 5'-ATACCAGGTACGCCTCCAGT-3'

634 To ensure no secondary mutations are present, the Papss ORF containing the correct mutations
635 was ligated with the original backbone of the UAS-Papss construct. The construct containing
636 both the K193A and F593P mutations was generated by combining DNA fragments containing
637 each mutation, which were obtained by digesting the respective K193A and F593P constructs,
638 and ligating them to a UAS backbone. Midi-prepped DNA samples were sent to GenetiVision
639 (Houston, TX) for a PhiC31 injection.

640

641 **Immunostaining and confocal microscopy**

642 *Drosophila* embryos were collected on a grape juice agar plate. All embryos were dechorionated
643 by incubation in 50% bleach for three minutes at room temperature. After dechorionation,
644 embryos were fixed in either saturated heptane or standard formaldehyde fixative (7 ml heptane,
645 5.6 ml ddH_2O, 700 µl 37% formaldehyde, 700 µl 10x PBS). Saturated heptane was prepared by

646 mixing heptane:37% formaldehyde 1:1 and shaking vigorously. For immunofluorescence
647 staining, embryos were fixed in saturated heptane for forty minutes at room temperature,
648 devitellinized by vortexing in 80% ethanol, and then washed three times in absolute ethanol. For
649 staining using the horseradish peroxidase (HRP) reaction for visualization, embryos were fixed
650 in formaldehyde fixative and devitellinized by vortexing in 100% methanol. Embryos were then
651 stained with primary and secondary antibodies in PBSTB (1X PBS, 0.2% bovine serum albumin,
652 and 0.1% Triton X-100). All antibodies used are listed in Table S3. Embryos were then mounted
653 in Aqua-Poly/Mount (Polysciences, Inc). Confocal images were taken using a Leica TCS SP8
654 confocal microscope with 63x, NA 1.4 and 40x, NA 1.3 objectives. HRP images were taken
655 using a Leica DM2500 microscope using a 20x, 0.8 NA objective.

656

657 **Fluorescence in-situ hybridization**

658 In situ hybridization in WT embryos was performed as described in Knirr et al., 1999. Embryos were
659 fixed in a standard formaldehyde fixation, followed by devitellinzation by 100% methanol. To make the
660 *Papss* mRNA probe that detects all splice forms, a 799 bp portion of the *Papss* ORF was amplified
661 using the *UAS-Papss-PD* construct as a template. To make isoform-specific mRNA probes, unique
662 sequence segments common to specific *Papss* isoforms were identified using Flybase sequences and
663 used to design primers for PCR amplification, using WT genomic DNA as a template. The primers are
664 listed below.

665

Papss isoform	Primer sequence	Product size
All isoforms	Forward Primer: 5'-ACAAGGATGCGGGTCTGAAG-3' Reverse Primer: 5'-G<u>ATTTGGTGACACTATAG</u>CGCCTTAACTCGTTGGGAG-3'	799 bp
ABCFG	Forward primer: 5'-	106 bp

	TTCGCAGTTTTGTTTGGAAT-3’ Reverse primer: 5'- GATTTAGGTGACACTATAGTGCTCTCCGG AACTTCACTCAT-3'	
EFH	Forward primer: 5'- TTCGCTTTCGACGTTCGTCG-3' Reverse primer: 5'- GATTTAGGTGACACTATAGCTTCTTTTGA TATGGGGATAAAA-3'	228 bp
DH	Forward primer: 5'- TTCACCTGCCCAACGTTTCG-3' Reverse primer: 5'- GATTTAGGTGACACTATAGCAAGCGCTGT TGTTATTGTTAA-3'	106 bp

666 *SP6 RNA polymerase promoter sequence underlined

667

668 Digoxigenin (DIG)-labeled RNA probe was generated by transcribing amplified and purified
669 DNA using SP6 RNA polymerase and DIG RNA labeling mix (Sigma). Following hybridization,
670 the RNA probe was detected using a sheep α-DIG antibody (Enzo; ENZ-ABS302-0001;
671 1:1,000). The secondary antibody, α-sheep IgG conjugated with biotin (Invitrogen; 1:500), was
672 visualized using a tyramide reaction with Cy3 (Perkin Elmer Life Sciences, NEL753001kt;
673 1:50). The embryos were mounted in Aqua-Poly/Mount. Confocal images were taken using a
674 Leica TCS SP8 confocal microscope with 63x, NA 1.4 and 40x, NA 1.3 objectives.

675

676 **Genomic DNA sequencing of the Papss open reading frame region in *Papss*^{2} mutant**

677 *Papss*^{2} homozygous mutant embryos were sorted for GFP signals in the balancer chromosome, and
678 genomic DNA was extracted from them. The open reading frame of *Papss* was amplified using the
679 isolated genomic DNA as a template, with the following primers.

680 Primer forward *Papss*: 5'-CTACAGGTGGCGACGAATGT-3'

681 Primer reverse *Papss*: 5'-GCGGCAGGTTCTGGTAGTAG-3'

682 Sanger sequencing of the amplified DNA segment of *Papss* was performed using the primers
683 below.

684 Forward primer 1: 5'-ACAGGTGGCGACGAATGTG-3'
685 Forward primer 2: 5'-TGACCGAGCAAAAGCACCAT-3'
686 Forward primer 3: 5'-CGAGGTGGCCAAGTTGTTTG-3'
687 Forward primer 4: 5'-CCCGAGTTCTACTTTCAGCGT-3'
688 Forward primer 5: 5'-GCCGGTGCGAACTTCTACAT-3'
689 Reverse primer: 5'-GCGGCAGGTTCTGGTAGTAG-3'
690

691 **Quantification of SG cell number**

692 Confocal images immunolabeled with CrebA for stage 16 SGs were used. 3D images for SGs were
693 generated using Imaris (Andor), and SG nuclei were counted using cell ID numbers. Data were
694 displayed using GraphPad Prism, and statistical significance was determined by one-way ANOVA.

695

696 **Quantification of SG lumen area**

697 Confocal images immunolabeled with Ecad for stage 16 SGs were used. Z-stacks were merged to
698 encompass the entirety of the SG lumen. Using Fiji (NIH), images were set to scale according to image
699 properties listed in LasX files. The polygon selection tool was used to outline the entirety of the SG
700 lumen, excluding the SG duct. SG lumen areas were determined for WT, *Papss* thin, and *Papss*
701 irregularly expanded respectively. Statistical significance was determined using a nonparametric t-test as
702 the data did not fit a Gaussian distribution. Sample numbers are: n=16, WT; n=13, $Papss^2$ with a thin
703 lumen; n=11, $Papss^2$ with an irregularly expanded lumen; n=8, $Papss^2/Df$ with a thin lumen; n=8,
704 $Papss^2/Df$ with a irregularly expanded lumen; n=10, *sage>Papss* with a normally expanded lumen; n=8,
705 *sage>Papss-PE;* $Papss^2$ with a normally expanded lumen; n=10, *sage>Papss-PD;* $Papss^2$ with a

706 normally expanded lumen; n=11, *sage>Papss-PD*^{K193A,F593P}*; Papss*^{2} with a thin lumen; n=7,
707 *sage>Papss-PD*^{K193A,F593P}*; Papss*^{2} with a irregularly expanded lumen.

708

709 **Quantification of SG lumen length and diameter**

710 Confocal images of stage 16 SGs immunolabeled with an antibody for the cell junction marker, E-cad,
711 were used. Several Z-sections, spanning approximately half of the circumferential/radial axis of the SG
712 lumen, were merged to create a projection which covered the entire length of the lumen. The line tool in
713 Fiji was used to measure the length of the SG lumen. To measure the diameter of the SG lumen, the
714 lumen was divided into four equal segments using the lumen length obtained above, as there are
715 sometimes minor variations in width value along the length of the lumen. The line tool in Fiji was then
716 used to measure the width along each quarter of the lumen, and an average value was obtained per SG.
717 Each measurement obtained in Fiji was adjusted for scale according to the image properties in the raw
718 confocal file. Sample numbers are: n=8, WT; n=8, *Papss*^{2} with a thin lumen; n=10, *Papss*^{2} with an
719 irregularly expanded lumen; n=8, *Papss*^{2}*/Df* with a thin lumen; n=8, *Papss*^{2}*/Df* with a irregularly
720 expanded lumen; n=10, *sage>Papss-PE* with a normally expanded lumen; n=8, *sage>Papss-PE; Papss*^{2}
721 with a normally expanded lumen; n=10 *sage>Papss-PD; Papss*^{2} with a normally expanded lumen;
722 n=11, *sage>Papss-PD*^{K193A,F593P}*; Papss*^{2} with a thin lumen; n=7, *sage>Papss-PD*^{K193A,F593P}*; Papss*^{2} with
723 a irregularly expanded lumen.

724

725 **Quantification of Crb signal intensity**

726 Confocal images of stage 16 SGs immunolabeled with antibodies against the sub-apical region (SAR)
727 marker, Crb, and the AJ marker, Ecad, were used. A maximum intensity projection of the apical region
728 of several SG cells with the highest Ecad and Crb signals was created using seven z-sections. Regions
729 were manually drawn along the inner or outer boundary of the Ecad signals of each cell to mark the
730 SAR and apical-medial regions. The mean gray value of the apical-medial Crb signals in each cell (the
731 region delineated by the inner boundary of the Ecad signals) was quantified using Fiji. The mean gray
732 value of the SAR Crb signals was calculated using the integrated densities and areas calculated with Fiji
733 for regions between inner and outer boundaries. To subtract the background, the average mean gray

734 value of Crb signals for five regions outside the embryo was subtracted from the mean gray values of the
735 SAR and apical-medial Crb signals in each SG cell. The ratio of the SAR to the apical-medial Crb level
736 was compared. Seven and six embryos were used for the WT and *Papss* mutants, respectively, and four
737 to eight cells per SG. SuperPlots were used to address variability in the data sets of each SG. Statistical
738 significance was determined using a Welch's t-test.

739

740 **Quantification of the number and signal intensity of WGA puncta**

741 High-resolution confocal images of stage 16 SGs immunostained with CrebA (SG nuclei), Ecad, and
742 WGA were obtained using an Olympus SpinSR10 Sora spinning disk confocal microscope with a 100x,
743 NA 1.5 objective. Each image was taken under identical imaging conditions. Three-dimensional (3D)
744 reconstruction of the WGA puncta was obtained using the Imaris software (Andor), and the number of
745 puncta per SG was counted by Imaris. The Imaris machine learning tool was used to exclude non-puncta
746 WGA signals within the SG and non-SG WGA puncta. After 3D reconstruction, the pixel intensity of
747 each WGA punctum was also obtained and used for further analysis.

748

749 **Quantification of WGA and ManII-GFP signal intensity**

750 Confocal images of stage 16 SGs immunostained for WGA and ManII-GFP were used. Single z-sections
751 of each image were imported into Fiji, and a line intensity profile was generated using the Line Tool and
752 Color Profiler pluggin. Lines were drawn across regions spanning two ManII-GFP/WGA puncta, and
753 the signal intensities for each pixel along the line for both ManII-GFP and WGA channels were
754 obtained.

755

756 **Quantification for Rab11 and Sec15 apical region intensity**

757 Single z-sections halfway through the proximal-distal axis from confocal images for stage 16 SGs
758 immunolabeled for Rab11 or Sec15 and Ecad were used for quantification. Threshold images for Sec15
759 or Rab11, which display pixels as black or white based on whether they are above a value for signal
760 intensity, were generated in Adobe Photoshop. In addition, Sec15 and Rab11 images were converted

761 using the RGB stack function in Fiji. A stack of images including the threshold and RGB stack
762 converted images for Sec15 or Rab11 and the Ecad images was generated using the images to stack
763 function in Fiji. Using the threshold images for Sec15 and Rab11, a boundary for the apical region
764 encompassing five SG cells, and the mean gray value intensity was calculated from the RGB stack
765 converted Rab11or Sec15 images. The graph was generated in GraphPad Prism, and statistical
766 significance was calculated using Welch's t-test.

767

768 **Quantification for Rab7 puncta number and intensity**

769 Single z-sections halfway through the proximal-distal axis from confocal images for stage 16 SGs
770 immunolabeled for Rab7 and Ecad were used for quantification. Threshold images for Rab7, which
771 display pixels as black or white based on whether they are above a value for signal intensity, were
772 generated in photoshop. Rab7 images were converted using the RGB stack function in Fiji. A stack of
773 images including the threshold and RGB stack converted images for Rab7 and Ecad images were
774 generated using the images to stack function in Fiji. Using the threshold images for Rab7, a boundary
775 was drawn around all puncta present in five cells for each sample, and the mean gray value intensity and
776 area was calculated for the RGB stack Rab7 converted image. The average mean gray value of punctate
777 intensity and the average number of punta in each cell were calculated using Fiji. Punta with an area
778 greater than or equal to 0.100 μm^2 were used for quantification. Statistical significance was calculated
779 by Welch's t-test using GraphPad Prism.

780

781 **Quantification of the number of dying cells**

782 Confocal images of stage 16 SGs that were immunolabeled with antibodies against CrebA (to mark the
783 SG nucleus), and DCP-1 (a cell death marker) were used. The number of regions within the SG with
784 DCP-1 signals and/or blank spots where CrebA signals should have been present were counted
785 manually.

786

787 **Transmission electron microscopy (TEM)**

788 Stage 15 embryos were fixed in 2% glutaraldehyde in 0.2 M phosphate buffer pH 7.4 and rinsed
789 4 times in 0.1 M phosphate buffer pH 7.2 containing 0.02 M glycine. Embryos were post-fixed in
790 2% osmium tetroxide for 1 hour in the dark, rinsed 3 times in dH_2O, stained en bloc in 1% uranyl
791 acetate for 1 hour in the dark, and rinsed 3 times in dH_2O. Samples were dehydrated in a series
792 of ethanol and then propylene oxide twice. Embryos were then infiltrated in propylene oxide:
793 Epon resin series and embedded in Epon at 60ºC for 24 hours. Semi-thin sections were
794 performed followed by Toluidine Blue staining to obtain a salivary gland section. Ultra-thin
795 sections for TEM were cut on a Leica EM UC7 microtome. TEM sections were mounted on
796 carbon-coated copper grids (EMS FCF-150-CU), stained with 2% uranyl acetate and Reynolds
797 lead citrate, and the ultra-thin sections were viewed on a JEOL JEM-1400, 120kV transmission
798 electron microscope and imaged with a Gatan digital camera. Sections from at least five
799 independent embryos were analyzed for wild type and *Papss* mutants.

800

801 **Figure legends**

802 **Figure 1. *Papss* mutants show defects in SG lumen expansion.** (A) Stage 16 SGs
803 immunostained for Stranded at Second (SAS). (B) In situ hybridization using an antisense probe
804 for *Papss* mRNA in WT embryos. (C-H) Stage 14 and stage 16 SGs immunostained for Ecad
805 and CrebA. Yellow asterisks indicate regions of irregular, non-uniform expansion (D, E, H) or
806 over-expansion (G) of the SG lumen. (I, I') Quantification of different SG lumen phenotypes. (J)
807 Quantification of SG lumen length. n=7-11 SGs for each genotype. See the Materials and
808 Methods for the sample size of each genotype. One-way ANOVA test with multiple comparison
809 (*, $p<0.05$; ns, non-significant). (K, K') Quantification of the SG lumen diameter (K) and the
810 coefficient of variation for each SG (K'). The diameter is measured in three different regions of
811 the lumen. The average diameter, as well as the individual data points, are shown. The same
812 samples are used for the quantifications in J-K'. One-way ANOVA test with multiple
813 comparison (***, $p<0.001$; ns, non-significant) (L) Quantification of SG lumen area. n=7-16
814 SGs for each genotype. One-way ANOVA test with multiple comparison (***, $p<0.001$; ****,
815 $p<0.0001$; ns, non-significant). Horizontal lines indicate mean values.

816 **Figure 2. Mutations in *Papss* result in mislocalized Crb and disruption of the aECM**
817 **architecture.** (A) Cartoon showing the subcellular localization of Crb in SG cells. (B, C) Stage
818 16 SGs immunostained for Crb and Ecad. Magnified images are shown for yellow dotted boxed
819 regions. (D) Quantification of the Crb signal intensity ratio between the SAR and apical-medial
820 regions of SG cells. (n=7, WT; n=6, $Papss^2$ (4-8 cells per SG)). Student's T-test with Welch's
821 correction (***, $p<0.001$). (E-G) Stage 16 SGs stained for Ecad and wheat germ agglutinin
822 (WGA). Magnified images are shown for the boxed regions. Arrows, WGA localization at the
823 apical membrane in WT (yellow) and *Papss* mutant (cyan) SGs. Yellow arrowhead in E, WGA
824 localizes as thin filaments in the lumen of WT SG. Cyan arrowheads, WGA localizes as a highly
825 condensed structure in the thin luminal region of the *Papss* SG. White arrowheads, WGA
826 localizes as a condensed, filamentous structure in the expanded luminal region of the *Papss* SG.
827 Yellow arrowheads in G, WGA localizes as a mildly condensed filament in the lumen of
828 *sage>Papss-PE;* $Papss^2$ SG. (H, I) TEM images of stage 15 SGs. SGs are pseudo-colored in
829 magenta. Magnified images of the luminal areas (boxed regions) are shown in the bottom.
830 Yellow asterisk in H, electron-dense luminal material in WT SG. Cyan asterisks in I, condensed

electron-dense luminal material in the *Papss* mutant SG. Green asterisk, a large luminal area lacking electron-dense material in the *Papss* mutant SG.

Figure 3. Loss of *Papss* results in disorganized Golgi structures and defects in intracellular trafficking components. (A-D) Stage 16 SGs stained with WGA. Magnified images are shown for the boxed regions. Yellow arrows, WGA signals as cytoplasmic puncta. Cyan arrows, WGA signals in the nuclear envelope. (E-H) Three-dimensional (3D) reconstruction of cytoplasmic WGA puncta in stage 16 SGs. (I, I') Quantification of the number of WGA puncta (I) and signal intensity (I') within SG cells. n=5 SGs for all genotypes, except WT in G (n=6). One-way ANOVA test with multiple comparisons (**, $p<0.01$; ***, $p<0.001$; ns, non-significant). Horizontal lines indicate mean values. (J, K) Stage 16 SGs stained for GFP (for ManII-GFP) and WGA. Magnified images are shown for the boxed regions. Yellow arrows in J, ManII-GFP and WGA puncta colocalize in WT SG. Asterisks in K, dispersed ManII-GFP signals in *Papss* mutants. Cyan arrows in K, little colocalization of ManII-GFP and WGA in the *Papss* SG. (L, L') Line intensity profile showing the signal intensity of ManII-GFP (green) and WGA (magenta) along the yellow and cyan dotted lines in J and K, respectively. (M, N) TEM images of the Golgi. Yellow arrows in M, Golgi structures in WT SG cells. Magenta arrows in N, Golgi structures in the *Papss* SG. Cyan arrows in N, electron-dense structures in the Golgi of *Papss* mutant SG cells. (O, P) Stage 16 SGs immunostained for Rab11 and Ecad. Magnified images are shown for boxed regions. Rab11 signals at the apical membrane are increased in *Papss* mutants (cyan arrowheads in P) compared to WT (yellow arrowheads in O), with occasional large punctate signals mislocalized to the basolateral domain (cyan arrow in P). (Q, R) Stage 16 SGs immunostained for Sec15 and Ecad. Compared to strong apical Sec15 signals in the WT SG (yellow arrowheads in Q), Sec15 signals are reduced in *Papss* mutants (cyan arrowheads in R). (S, T) Quantification of the intensity of Rab11 (S) and Sec15 (T) at the apical membrane regions in WT and *Papss* mutant SGs. Welch's t-test (**, $p<0.05$). Horizontal lines indicate mean values. (U, V) TEM images for the apical region of SG cells. Yellow arrowheads, electron-dense vesicles in both genotypes. Red arrowheads, empty, larger vesicle-like structures in *Papss* mutants. (W) Quantification of the electron-dense vesicle numbers per cell slice. Welch's t-test (**, $p<0.05$). Horizontal lines indicate mean values.

861 **Figure 4. *Papss* mutants show premature SG cell death.** (A, B) Stage 16 SGs immunostained
862 for CrebA, DCP-1 and Ecad. Cross-sectional images are shown for the yellow dashed line in B.
863 Yellow arrowheads, DCP-1 signal is detected in the SG in *Papss* mutants. White dashed lines,
864 the basal boundary of the SG. (C) TEM image of stage 15 SG cells, including a dying cell
865 (yellow arrow). Cyan arrows, nuclei of normal living cells. (D) Quantification of the number of
866 acellular regions in stage 16 SGs. (n=8 SGs, WT; n=10, $Papss^2$; n=15, *sage>Papss-PD;* $Papss^2$;
867 n=8, *sage>Papss-PD*^{K193A,F593P}; $Papss^2$) (E) Quantification of the number of SG cells at stage 16
868 (n=10 SGs, WT; n=10, $Papss^2$; n=8, $Papss^2$/*Df*; n=8, *sage>p35;* $Papss^2$; n=10, *sage>Papss-PE;*
869 $Papss^2$; n=8, *sage>Papss-PD*^{K193A,F593P}; $Papss^2$). One way ANOVA test (****, $p<0.0001$; ns,
870 non-significant). (F, G) Stage 16 SGs immunostained for CrebA, Ecad, and mCherry (for
871 Hemo3x-mCh). Cross-section images are shown for the yellow dashed lines. White dashed lines,
872 the basal boundary of the SG. Yellow arrowhead in F, hemocyte signals outside of the control
873 SG. White arrowhead in G, hemocyte signals are present inside the SG in *Papss* mutants. (H, I)
874 Stage 16 SGs immunostained for DAPI, mCh (for Hemo3x-mCh), and Ndg. Magnified views are
875 shown for boxed regions. Yellow dashed lines, the basal boundary of the SG. (H) In WT,
876 hemocytes are found outside of the SG (yellow arrowheads), with Ndg forming a barrier at the
877 basal boundary of the SG (yellow arrows). (I) In *Papss* mutants, hemocytes invade the SG
878 epithelia (white arrowheads), where Ndg signals are irregular or absent (white arrows).

879 **Figure 5. Loss of *Papss* disrupts the localization of Dpy and Pio in the aECM.** (A) Stage 16
880 SGs stained for a chitin-binding protein (CBP) and Ecad. (B) Cartoon of the mCh-Pio fusion
881 protein showing the region for the antibody and protease cleavage sites. (C, D) Stage 14 and
882 stage 16 SGs immunostained for mCh (for mCh-Pio) and GFP (for Dpy-YFP). The mCh-Pio
883 (white arrowheads) and Dpy-YFP (cyan arrowheads) signals are largely absent from the
884 expanded region of the lumen. Along one side of the lumen, weak mCh-Pio signals colocalize
885 with condensed Dpy-YFP signals (yellow arrows). (E-H’’’) Stage 14 and stage 16 SGs
886 immunostained for Pio, GFP, and Ecad. Magnified images of boxed regions in E-H and shown in
887 E’-H’’. F’’ and H’’’ are cross-sectional images of the SG lumen for regions indicated by white
888 lines F’ and H’’. Yellow arrowheads, Pio and Dpy localized to the apical membrane. Cyan
889 arrowheads, Dpy and Pio localized to the SG lumen. Note a higher proportion of Dpy and Pio
890 localized to the lumen in the *Papss* mutant SG at stage 14 (cyan arrowheads in G’). White

891 arrowheads in H'-H''', Dpy accumulates towards one side of the lumen in the stage 16 *Papss*
892 SG. Yellow asterisks, Pio is absent from the lumen at stage 16 in the *Papss* SG.

893 **Figure 6. Pio is essential for uniform SG lumen diameter by maintaining Dpy in the lumen.**
894 (A, B) SGs at stages 13-16 stained for WGA and Ecad. Yellow arrowheads in A, filamentous
895 luminal WGA signals. Cyan arrowheads in B, WGA signals at the apical membrane. Yellow
896 asterisks, loss of lumina WGA signals. White arrowheads, constricted lumen. (C) Stage 16 SGs
897 immunostained for Ecad and CrebA. Cross sectional images for the yellow and green dotted
898 lines are shown on the right. Yellow arrowhead, flat protrusion of the lumen. Green arrowhead,
899 constricted lumen. (D) Stage 16 SGs stained for Ecad and GFP (for Dpy-YFP). Projection
900 images contain merged z-sections, from the apical surface of the SG cells to midway through the
901 SG. Single section, one z-section at the approximate midpoint of the lumen width. Yellow
902 arrowhead, area of constricted lumen. Yellow asterisk, luminal area with no Dpy-YFP signals.
903 (E) Single z-sections of confocal images of SGs at stages 15 and 16 stained for Ecad, Pio and
904 WGA. White arrowheads, area of constricted lumen. Yellow asterisks, no luminal signals of
905 WGA and Pio. (F) Quantification of the number of constrictions in the SG lumen at stage 16
906 (n=7 for both genotypes). (G, G') SGs at stages 14-16 stained for Ecad, WGA and Pio. Higher
907 magnification of the yellow boxed regions is shown in G'. (H, I) Stage 16 SGs overexpressing
908 Np^{WT} (H) or Np^{mut} (I) that are immunostained for GFP (for Dpy-YFP and Np-GFP), Pio, and
909 mCh (for mCh-Pio). Np^{WT}-overexpressing SGs show strong, uniform mCh-Pio signals in the
910 lumen (cyan asterisks in H), whereas Np^{mut}-overexpressing SGs shows no detectable signals in
911 the lumen (cyan asterisk in I). In Np^{WT}-overexpressing SGs, the luminal mCh-Pio signals are so
912 bright that the cytoplasmic, punctate mCh-Pio signals are rarely detectable alongside the luminal
913 signals. Increasing the brightness to visualize the cytoplasmic punctate signals shows very strong
914 luminal mCh-Pio signals (inset in H). Np^{WT} overexpression shows high levels of Pio (magenta
915 arrowheads in H) and dpy-YFP (green arrowheads in H) signals in both the apical membrane and
916 lumen. In contrast, Np^{mut} overexpression shows strong Pio signals in the apical membrane and
917 various levels of Pio in the lumen. (I', I'') Higher magnification of the yellow boxed regions.
918 The lumen diameter of the region with undetectable luminal Pio levels is slightly larger (magenta
919 asterisk) compared to the region with clear luminal Pio signals (magenta arrowheads).

920

921 **Figure 7. A proposed model.** (A) Cartoon diagram showing normal lumen expansion in WT SG
922 and defective luminal morphology in *Papss*, *pio*, and *Np* mutants. (B) Organization of the ZP
923 domain protein-containing aECM in the SG. In WT, the ZP-C fragment of Pio (which is cleaved
924 by Np and furin proteases) forms a complex with Dpy to build a filamentous scaffold within the
925 lumen. In *Papss* mutants, this fragment is absent from the lumen at stage 16, and the Dpy-
926 containing aECM structure becomes aggregated and highly condensed. The absence of luminal
927 Pio in *pio* and *Np* mutants results in the loss of luminal Dpy and lumen constrictions.

928

Acknowledgements

We thank the members of the Chung laboratory for their comments and suggestions. We thank M. Behr, S. Hayashi, the Bloomington stock center (NIH P40OD018537), and the Kyoto *Drosophila* stock center at Kyoto Institute of Technology for fly stocks. We thank M. Affolter for the Pio antibody. Many antibodies were obtained from the Developmental Studies Hybridoma Bank, created by the NICHD of the NIH and maintained at The University of Iowa, Department of Biology, Iowa City, IA 52242. cDNAs for *Papss* were obtained from the *Drosophila* Genomics Resource Center (NIH 2P40OD010949). Confocal and electron microscopy were performed at the Shared Instrumentation Facility (SIF) at Louisiana State University. The model in Figure 7 was created in https://BioRender.com. This work was supported by the National Science Foundation (MCB 2141387) and National Institutes of Health (R03DE034704) to SC.

942 **Table S1. A targeted Df screen revealed Papss as a key enzyme for SG lumen expansion.**

SG-upregulated enzymes	Predicted roles	Df lines tested	SG lumen shape
CG17633	Metallocarboxypeptidase	Exel6024	Disrupted embryo morphology
CG30283	Serine-type endopeptidase	Exel6076	Disrupted embryo morphology
Papss	PAPS synthetase	Bsc445	Thin SG lumen with apical protrusions
PH4αSG1/SG2	Prolyl 4-hydroxylase	Exel6216	Non-uniform lumen diameter
CG16758	Purine nucleotide phosphorylase	Bsc116	Non-uniform lumen diameter
CG8708	N-acetylgalactosaminide β-1,3-galactosyltransferase	Exel7095	Irregular apical membrane
CG7920	Acetate CoA-transferase	Bsc620	Irregular apical membrane
Pgant6	Polypeptide N-acetylgalactosaminyltransferase	Exel6091	Irregular apical membrane
GlcAT-P	Glucuronosyltransferase	Bsc817	Irregular apical membrane
CG34290	Serine-type endopeptidase	Bsc638	Irregular apical membrane
Peroxidasin	Bromide peroxidase	Bsc119	Irregular apical membrane
ScsβG	Succinyl Co-A synthetase β subunit	Bsc387	Short and rounded SG

943

944 **Table S2. Fly strains used**

Fly strain	**Sources and References**	**RRID**
Oregon R (wild type)		
sage-Gal4	Chung et al., 2009	
fkh-Gal4	Henderson and Andrew, 2000	
Papss^{2}	Bloomington Stock Center	BDSC_26171
UAS-p35	Bloomington Stock Center	BDSC_5072
UAS-Papss-PD	This work	
UAS-Papss-PE	This work	
UAS-Papss-PD$^{K193A,\ F593F}$	This work	
Dpy-YFP	Kyoto stock center	DGGR_115238
SrpHemo3x-mCherry	Gyoergy et al., 2018	BDSC_78358
Dp-YFP, mCh-Qsm	Chu and Hayashi, 2021	
mCh-Qsm	Chu and Hayashi, 2021	
Dpy-YFP, mCh-Pio	Drees et al., 2023	
UAS-ManII-GFP	Bloomington stock center	BDSC_65248
UAS-GFP-KDEL	Bloomington stock center	BDSC_9898
pio^{17c}	Drees et al., 2023	
Np^{C2}	Drees et al., 2023	
dpy^{ov1}	Bloomington stock center	BDSC_276
Grasp65^{102}	Zhou et al., 2014	BDSC_65257
GM130$^{\Delta 23}$	Zhou et al., 2014	BDSC_65255

UAS-Np.WT-Strep	Drees et al., 2019	
UAS-Np.S990A-GFP	Drees et al., 2019	

945

946

947 **Table S3. Antibodies Used**

Antibody	Source	RRID	Dilution
α-Ecad (rat)	DSHB (DCAD2)	AB_528120	1:50
α-CrebA (rat)	Andrew lab (John Hopkins University); re-made in this study		1:3,000
α-CrebA (rabbit)	Andrew lab (John Hopkins University)	AB_10805295	1:5,000
α-CrebA (guinea pig)	This study		1:5,000
α-GFP (mouse)	Invitrogen (A11120)	AB_221568	1:500
α-GFP (chicken)	Invitrogen (A10262)	AB_2534023	1:1,000
α-RFP (rabbit)	Invitrogen (R10367)	AB_10563941	1: 2,000
α-β-galactosidase (rabbit)	Invitrogen (A11132)	AB_221539	1:500
α-β-galactosidase (mouse)	Invitrogen (MA5-15222)	AB_10980770	1:500
α-mCherry (rat)	Invitrogen (M11217)	AB_2536611	1:1,000
α-mCherry (rabbit)	Invitrogen (PA534974)	AB_2552323	1:1,000
α-DCP-1 (rabbit)	Cell signaling technology (9578)	AB_2721060	1:200
α-Crb (mouse)	DSHB (Cq4)	AB_528181	1:10
α-Rab11 (rabbit)	Andrew lab (John Hopkins University)		1:500
α-Rab7 (mouse)	DSHB (Rab7)	AB_2722471	1:10

α-Sec15 (guinea pig)	Bellen lab (Baylor College of Medicine)		1:2,000
α-α-Spectrin (mouse)	DSHB (3A9)	AB_528473	1:2
α-Discs large (mouse)	DSHB (4F3)	AB_528203	1:500
α-Pio (rabbit)	Affolter lab (Jaźwińska et al., 2003)		1:500
α-Nidogen (rabbit)	Holz lab (Wolfstetter et al., 2009)		1:2,000
α-Sulfotyrosine (mouse)	Sigma (ZMS1096-25UL)		1:50
Alexa Fluor 488/568/647-coupled secondary antibodies	Invitrogen		1:500

948

949 **References**

950 Abrams, E. W., Mihoulides, W. K., & Andrew, D. J. (2006). Fork head and Sage maintain a
951 uniform and patent salivary gland lumen through regulation of two downstream target
952 genes, PH4alphaSG1 and PH4alphaSG2. *Development*, *133*(18), 3517-3527.
953 https://doi.org/10.1242/dev.02525
954 Ahmad, M., Faiyaz Ul Haque, M., Ahmad, W., Abbas, H., Haque, S., Krakow, D., Rimoin, D.
955 L., Lachman, R. S., & Cohn, D. H. (1998). Distinct, autosomal recessive form of
956 spondyloepimetaphyseal dysplasia segregating in an inbred Pakistani kindred. *Am J Med*
957 *Genet*, *78*(5), 468-473. https://www.ncbi.nlm.nih.gov/pubmed/9714015
958 Araujo, S. J., Aslam, H., Tear, G., & Casanova, J. (2005). mummy/cystic encodes an enzyme
959 required for chitin and glycan synthesis, involved in trachea, embryonic cuticle and CNS
960 development--analysis of its role in Drosophila tracheal morphogenesis. *Dev Biol*,
961 *288*(1), 179-193. https://doi.org/10.1016/j.ydbio.2005.09.031
962 Bokel, C., Prokop, A., & Brown, N. H. (2005). Papillote and Piopio: Drosophila ZP-domain
963 proteins required for cell adhesion to the apical extracellular matrix and microtubule
964 organization. *J Cell Sci*, *118*(Pt 3), 633-642. https://doi.org/10.1242/jcs.01619
965 Bradley, P. L., & Andrew, D. J. (2001). ribbon encodes a novel BTB/POZ protein required for
966 directed cell migration in Drosophila melanogaster. *Development*, *128*(15), 3001-3015.
967 https://doi.org/10.1242/dev.128.15.3001
968 Bradley, P. L., Myat, M. M., Comeaux, C. A., & Andrew, D. J. (2003). Posterior migration of
969 the salivary gland requires an intact visceral mesoderm and integrin function. *Dev Biol*,
970 *257*(2), 249-262. https://doi.org/10.1016/s0012-1606(03)00103-9
971 Bulow, H. E., & Hobert, O. (2004). Differential sulfations and epimerization define heparan
972 sulfate specificity in nervous system development. *Neuron*, *41*(5), 723-736.
973 https://doi.org/10.1016/s0896-6273(04)00084-4
974 Chandrasekaran, V., & Beckendorf, S. K. (2003). senseless is necessary for the survival of
975 embryonic salivary glands in Drosophila. *Development*, *130*(19), 4719-4728.
976 https://doi.org/10.1242/dev.00677
977 Chu, W. C., & Hayashi, S. (2021). Mechano-chemical enforcement of tendon apical ECM into
978 nano-filaments during Drosophila flight muscle development. *Curr Biol*, *31*(7), 1366-
979 1378 e1367. https://doi.org/10.1016/j.cub.2021.01.010

980 Chung, S., & Andrew, D. J. (2014). Cadherin 99C regulates apical expansion and cell
981 rearrangement during epithelial tube elongation. *Development*, *141*(9), 1950-1960.
982 https://doi.org/10.1242/dev.104166
983 Chung, S., Hanlon, C. D., & Andrew, D. J. (2014). Building and specializing epithelial tubular
984 organs: the Drosophila salivary gland as a model system for revealing how epithelial
985 organs are specified, form and specialize. *Wiley Interdiscip Rev Dev Biol*, *3*(4), 281-300.
986 https://doi.org/10.1002/wdev.140
987 Chung, S., Kim, S., & Andrew, D. J. (2017). Uncoupling apical constriction from tissue
988 invagination. *Elife*, *6*. https://doi.org/10.7554/eLife.22235
989 Chung, S., Vining, M. S., Bradley, P. L., Chan, C. C., Wharton, K. A., Jr., & Andrew, D. J.
990 (2009). Serrano (sano) functions with the planar cell polarity genes to control tracheal
991 tube length. *PLoS Genet*, *5*(11), e1000746. https://doi.org/10.1371/journal.pgen.1000746
992 Cohen, J. D., Bermudez, J. G., Good, M. C., & Sundaram, M. V. (2020). A C. elegans Zona
993 Pellucida domain protein functions via its ZPc domain. *PLoS Genet*, *16*(11), e1009188.
994 https://doi.org/10.1371/journal.pgen.1009188
995 Cohen, J. D., Sparacio, A. P., Belfi, A. C., Forman-Rubinsky, R., Hall, D. H., Maul-Newby, H.,
996 Frand, A. R., & Sundaram, M. V. (2020). A multi-layered and dynamic apical
997 extracellular matrix shapes the vulva lumen in Caenorhabditis elegans. *Elife*, *9*.
998 https://doi.org/10.7554/eLife.57874
999 Devine, W. P., Lubarsky, B., Shaw, K., Luschnig, S., Messina, L., & Krasnow, M. A. (2005).
1000 Requirement for chitin biosynthesis in epithelial tube morphogenesis. *Proc Natl Acad Sci*
1001 *U S A*, *102*(47), 17014-17019. https://doi.org/10.1073/pnas.0506676102
1002 Diaz-Balzac, C. A., Lazaro-Pena, M. I., Tecle, E., Gomez, N., & Bulow, H. E. (2014). Complex
1003 cooperative functions of heparan sulfate proteoglycans shape nervous system
1004 development in Caenorhabditis elegans. *G3 (Bethesda)*, *4*(10), 1859-1870.
1005 https://doi.org/10.1534/g3.114.012591
1006 Dierker, T., Shao, C., Haitina, T., Zaia, J., Hinas, A., & Kjellen, L. (2016). Nematodes join the
1007 family of chondroitin sulfate-synthesizing organisms: Identification of an active
1008 chondroitin sulfotransferase in Caenorhabditis elegans. *Sci Rep*, *6*, 34662.
1009 https://doi.org/10.1038/srep34662

1010 Dong, B., Miao, G., & Hayashi, S. (2014). A fat body-derived apical extracellular matrix enzyme
1011 is transported to the tracheal lumen and is required for tube morphogenesis in Drosophila.
1012 *Development*, *141*(21), 4104-4109. https://doi.org/10.1242/dev.109975
1013 Drees, L., Konigsmann, T., Jaspers, M. H. J., Pflanz, R., Riedel, D., & Schuh, R. (2019).
1014 Conserved function of the matriptase-prostasin proteolytic cascade during epithelial
1015 morphogenesis. *PLoS Genet*, *15*(1), e1007882.
1016 https://doi.org/10.1371/journal.pgen.1007882
1017 Drees, L., Schneider, S., Riedel, D., Schuh, R., & Behr, M. (2023). The proteolysis of ZP
1018 proteins is essential to control cell membrane structure and integrity of developing
1019 tracheal tubes in Drosophila. *Elife*, *12*. https://doi.org/10.7554/eLife.91079
1020 Faiyaz ul Haque, M., King, L. M., Krakow, D., Cantor, R. M., Rusiniak, M. E., Swank, R. T.,
1021 Superti-Furga, A., Haque, S., Abbas, H., Ahmad, W., Ahmad, M., & Cohn, D. H. (1998).
1022 Mutations in orthologous genes in human spondyloepimetaphyseal dysplasia and the
1023 brachymorphic mouse. *Nat Genet*, *20*(2), 157-162. https://doi.org/10.1038/2458
1024 Ford-Hutchinson, A. F., Ali, Z., Seerattan, R. A., Cooper, D. M., Hallgrimsson, B., Salo, P. T., &
1025 Jirik, F. R. (2005). Degenerative knee joint disease in mice lacking 3'-phosphoadenosine
1026 5'-phosphosulfate synthetase 2 (Papss2) activity: a putative model of human PAPSS2
1027 deficiency-associated arthrosis. *Osteoarthritis Cartilage*, *13*(5), 418-425.
1028 https://doi.org/10.1016/j.joca.2004.12.011
1029 Fox, R. M., & Andrew, D. J. (2015). Changes in organelle position and epithelial architecture
1030 associated with loss of CrebA. *Biol Open*, *4*(3), 317-330.
1031 https://doi.org/10.1242/bio.201411205
1032 Fox, R. M., Vaishnavi, A., Maruyama, R., & Andrew, D. J. (2013). Organ-specific gene
1033 expression: the bHLH protein Sage provides tissue specificity to Drosophila FoxA.
1034 *Development*, *140*(10), 2160-2171. https://doi.org/10.1242/dev.092924
1035 Ghosh, N., & Treisman, J. E. (2024). Apical cell expansion maintained by Dusky-like establishes
1036 a scaffold for corneal lens morphogenesis. *Sci Adv*, *10*(34), eado4167.
1037 https://doi.org/10.1126/sciadv.ado4167
1038 Gill, H. K., Cohen, J. D., Ayala-Figueroa, J., Forman-Rubinsky, R., Poggioli, C., Bickard, K.,
1039 Parry, J. M., Pu, P., Hall, D. H., & Sundaram, M. V. (2016). Integrity of Narrow

1040 Epithelial Tubes in the C. elegans Excretory System Requires a Transient Luminal
1041 Matrix. *PLoS Genet*, *12*(8), e1006205. https://doi.org/10.1371/journal.pgen.1006205
1042 Groza, T., Gomez, F. L., Mashhadi, H. H., Munoz-Fuentes, V., Gunes, O., Wilson, R., Cacheiro,
1043 P., Frost, A., Keskivali-Bond, P., Vardal, B., McCoy, A., Cheng, T. K., Santos, L., Wells,
1044 S., Smedley, D., Mallon, A. M., & Parkinson, H. (2023). The International Mouse
1045 Phenotyping Consortium: comprehensive knockout phenotyping underpinning the study
1046 of human disease. *Nucleic Acids Res*, *51*(D1), D1038-D1045.
1047 https://doi.org/10.1093/nar/gkac972
1048 Gunal, S., Hardman, R., Kopriva, S., & Mueller, J. W. (2019). Sulfation pathways from red to
1049 green. *J Biol Chem*, *294*(33), 12293-12312. https://doi.org/10.1074/jbc.REV119.007422
1050 Gyoergy, A., Roblek, M., Ratheesh, A., Valoskova, K., Belyaeva, V., Wachner, S.,
1051 Matsubayashi, Y., Sanchez-Sanchez, B. J., Stramer, B., & Siekhaus, D. E. (2018). Tools
1052 Allowing Independent Visualization and Genetic Manipulation of Drosophila
1053 melanogaster Macrophages and Surrounding Tissues. *G3 (Bethesda)*, *8*(3), 845-857.
1054 https://doi.org/10.1534/g3.117.300452
1055 Herman, T., & Horvitz, H. R. (1999). Three proteins involved in Caenorhabditis elegans vulval
1056 invagination are similar to components of a glycosylation pathway. *Proc Natl Acad Sci U*
1057 *S A*, *96*(3), 974-979. https://doi.org/10.1073/pnas.96.3.974
1058 Hwang, H. Y., Olson, S. K., Brown, J. R., Esko, J. D., & Horvitz, H. R. (2003). The
1059 Caenorhabditis elegans genes sqv-2 and sqv-6, which are required for vulval
1060 morphogenesis, encode glycosaminoglycan galactosyltransferase II and
1061 xylosyltransferase. *J Biol Chem*, *278*(14), 11735-11738.
1062 https://doi.org/10.1074/jbc.C200518200
1063 Ismat, A., Cheshire, A. M., & Andrew, D. J. (2013). The secreted AdamTS-A metalloprotease is
1064 required for collective cell migration. *Development*, *140*(9), 1981-1993.
1065 https://doi.org/10.1242/dev.087908
1066 Jazwinska, A., & Affolter, M. (2004). A family of genes encoding zona pellucida (ZP) domain
1067 proteins is expressed in various epithelial tissues during Drosophila embryogenesis. *Gene*
1068 *Expr Patterns*, *4*(4), 413-421. https://doi.org/10.1016/j.modgep.2004.01.003

1069 Jazwinska, A., Ribeiro, C., & Affolter, M. (2003). Epithelial tube morphogenesis during
1070 Drosophila tracheal development requires Piopio, a luminal ZP protein. *Nat Cell Biol*,
1071 *5*(10), 895-901. https://doi.org/10.1038/ncb1049
1072 Jovine, L., Darie, C. C., Litscher, E. S., & Wassarman, P. M. (2005). Zona pellucida domain
1073 proteins. *Annu Rev Biochem*, *74*, 83-114.
1074 https://doi.org/10.1146/annurev.biochem.74.082803.133039
1075 Jovine, L., Qi, H., Williams, Z., Litscher, E., & Wassarman, P. M. (2002). The ZP domain is a
1076 conserved module for polymerization of extracellular proteins. *Nat Cell Biol*, *4*(6), 457-
1077 461. https://doi.org/10.1038/ncb802
1078 Jullien, D., Crozatier, M., & Kas, E. (1997). cDNA sequence and expression pattern of the
1079 Drosophila melanogaster PAPS synthetase gene: a new salivary gland marker. *Mech Dev*,
1080 *68*(1-2), 179-186. https://doi.org/10.1016/s0925-4773(97)00136-6
1081 Kamiyama, S., Suda, T., Ueda, R., Suzuki, M., Okubo, R., Kikuchi, N., Chiba, Y., Goto, S.,
1082 Toyoda, H., Saigo, K., Watanabe, M., Narimatsu, H., Jigami, Y., & Nishihara, S. (2003).
1083 Molecular cloning and identification of 3'-phosphoadenosine 5'-phosphosulfate
1084 transporter. *J Biol Chem*, *278*(28), 25958-25963.
1085 https://doi.org/10.1074/jbc.M302439200
1086 Karlsson, M., Zhang, C., Mear, L., Zhong, W., Digre, A., Katona, B., Sjostedt, E., Butler, L.,
1087 Odeberg, J., Dusart, P., Edfors, F., Oksvold, P., von Feilitzen, K., Zwahlen, M., Arif, M.,
1088 Altay, O., Li, X., Ozcan, M., Mardinoglu, A.,…Lindskog, C. (2021). A single-cell type
1089 transcriptomics map of human tissues. *Sci Adv*, *7*(31).
1090 https://doi.org/10.1126/sciadv.abh2169
1091 Kinnunen, T., Huang, Z., Townsend, J., Gatdula, M. M., Brown, J. R., Esko, J. D., & Turnbull, J.
1092 E. (2005). Heparan 2-O-sulfotransferase, hst-2, is essential for normal cell migration in
1093 Caenorhabditis elegans. *Proc Natl Acad Sci U S A*, *102*(5), 1507-1512.
1094 https://doi.org/10.1073/pnas.0401591102
1095 Kondylis, V., & Rabouille, C. (2009). The Golgi apparatus: lessons from Drosophila. *FEBS Lett*,
1096 *583*(23), 3827-3838. https://doi.org/10.1016/j.febslet.2009.09.048
1097 Kurima, K., Warman, M. L., Krishnan, S., Domowicz, M., Krueger, R. C., Jr., Deyrup, A., &
1098 Schwartz, N. B. (1998). A member of a family of sulfate-activating enzymes causes

1099 murine brachymorphism. *Proc Natl Acad Sci U S A*, *95*(15), 8681-8685.
1100 https://doi.org/10.1073/pnas.95.15.8681
1101 Le, T. P., & Chung, S. (2021). Regulation of apical constriction via microtubule- and Rab11-
1102 dependent apical transport during tissue invagination. *Mol Biol Cell*, *32*(10), 1033-1047.
1103 https://doi.org/10.1091/mbc.E21-01-0021
1104 Legan, P. K., Rau, A., Keen, J. N., & Richardson, G. P. (1997). The mouse tectorins. Modular
1105 matrix proteins of the inner ear homologous to components of the sperm-egg adhesion
1106 system. *J Biol Chem*, *272*(13), 8791-8801. https://doi.org/10.1074/jbc.272.13.8791
1107 Litscher, E. S., & Wassarman, P. M. (2020). Zona pellucida genes and proteins and human
1108 fertility. *Trends Dev Biol*, *13*, 21-33. https://www.ncbi.nlm.nih.gov/pubmed/33335361
1109 Luders, F., Segawa, H., Stein, D., Selva, E. M., Perrimon, N., Turco, S. J., & Hacker, U. (2003).
1110 Slalom encodes an adenosine 3'-phosphate 5'-phosphosulfate transporter essential for
1111 development in Drosophila. *EMBO J*, *22*(14), 3635-3644.
1112 https://doi.org/10.1093/emboj/cdg345
1113 Luschnig, S., Batz, T., Armbruster, K., & Krasnow, M. A. (2006). serpentine and vermiform
1114 encode matrix proteins with chitin binding and deacetylation domains that limit tracheal
1115 tube length in Drosophila. *Curr Biol*, *16*(2), 186-194.
1116 https://doi.org/10.1016/j.cub.2005.11.072
1117 Lye, C. M., Naylor, H. W., & Sanson, B. (2014). Subcellular localisations of the CPTI collection
1118 of YFP-tagged proteins in Drosophila embryos. *Development*, *141*(20), 4006-4017.
1119 https://doi.org/10.1242/dev.111310
1120 Matthew, J., Vishwakarma, V., Le, T. P., Agsunod, R. A., & Chung, S. (2024). Coordination of
1121 cell cycle and morphogenesis during organ formation. *Elife*, *13*.
1122 https://doi.org/10.7554/eLife.95830
1123 McAllister, K. A., Grogg, K. M., Johnson, D. W., Gallione, C. J., Baldwin, M. A., Jackson, C.
1124 E., Helmbold, E. A., Markel, D. S., McKinnon, W. C., Murrell, J., & et al. (1994).
1125 Endoglin, a TGF-beta binding protein of endothelial cells, is the gene for hereditary
1126 haemorrhagic telangiectasia type 1. *Nat Genet*, *8*(4), 345-351.
1127 https://doi.org/10.1038/ng1294-345

1128 Mei, Z., Kuzhir, P., & Godeau, G. (2024). Update on Chitin and Chitosan from Insects: Sources,
1129 Production, Characterization, and Biomedical Applications. *Biomimetics (Basel)*, *9*(5).
1130 https://doi.org/10.3390/biomimetics9050297
1131 Moussian, B., Tang, E., Tonning, A., Helms, S., Schwarz, H., Nusslein-Volhard, C., & Uv, A. E.
1132 (2006). Drosophila Knickkopf and Retroactive are needed for epithelial tube growth and
1133 cuticle differentiation through their specific requirement for chitin filament organization.
1134 *Development*, *133*(1), 163-171. https://doi.org/10.1242/dev.02177
1135 Mueller, J. W., & Shafqat, N. (2013). Adenosine-5'-phosphosulfate--a multifaceted modulator of
1136 bifunctional 3'-phospho-adenosine-5'-phosphosulfate synthases and related enzymes.
1137 *FEBS J*, *280*(13), 3050-3057. https://doi.org/10.1111/febs.12252
1138 Myat, M. M., & Andrew, D. J. (2000a). Fork head prevents apoptosis and promotes cell shape
1139 change during formation of the Drosophila salivary glands. *Development*, *127*(19), 4217-
1140 4226. https://doi.org/10.1242/dev.127.19.4217
1141 Myat, M. M., & Andrew, D. J. (2000b). Organ shape in the Drosophila salivary gland is
1142 controlled by regulated, sequential internalization of the primordia. *Development*, *127*(4),
1143 679-691. https://doi.org/10.1242/dev.127.4.679
1144 Op De Beeck, K., Vermeire, S., Rutgeerts, P., & Bossuyt, X. (2012). Antibodies to GP2, the
1145 major zymogen granule membrane glycoprotein, in inflammatory bowel diseases. *Gut*,
1146 *61*(1), 162-164; author reply 164-165. https://doi.org/10.1136/gut.2010.233148
1147 Plaza, S., Chanut-Delalande, H., Fernandes, I., Wassarman, P. M., & Payre, F. (2010). From A to
1148 Z: apical structures and zona pellucida-domain proteins. *Trends Cell Biol*, *20*(9), 524-
1149 532. https://doi.org/10.1016/j.tcb.2010.06.002
1150 Porter, K. R., & Tamm, I. (1955). Direct visualization of a mucoprotein component of urine. *J*
1151 *Biol Chem*, *212*(1), 135-140. https://www.ncbi.nlm.nih.gov/pubmed/13233216
1152 Renner, M., Bergmann, G., Krebs, I., End, C., Lyer, S., Hilberg, F., Helmke, B., Gassler, N.,
1153 Autschbach, F., Bikker, F., Strobel-Freidekind, O., Gronert-Sum, S., Benner, A., Blaich,
1154 S., Wittig, R., Hudler, M., Ligtenberg, A. J., Madsen, J., Holmskov, U.,…Mollenhauer, J.
1155 (2007). DMBT1 confers mucosal protection in vivo and a deletion variant is associated
1156 with Crohn's disease. *Gastroenterology*, *133*(5), 1499-1509.
1157 https://doi.org/10.1053/j.gastro.2007.08.007

1158 Rutherford, S. A., Goldberg, M. W., & Allen, T. D. (1997). Three-dimensional visualization of
1159 the route of protein import: the role of nuclear pore complex substructures. *Exp Cell Res*,
1160 *232*(1), 146-160. https://doi.org/10.1006/excr.1997.3487
1161 Sarkissian, T., Timmons, A., Arya, R., Abdelwahid, E., & White, K. (2014). Detecting apoptosis
1162 in Drosophila tissues and cells. *Methods*, *68*(1), 89-96.
1163 https://doi.org/10.1016/j.ymeth.2014.02.033
1164 Smith, S. J., Davidson, L. A., & Rebeiz, M. (2020). Evolutionary expansion of apical
1165 extracellular matrix is required for the elongation of cells in a novel structure. *Elife*, *9*.
1166 https://doi.org/10.7554/eLife.55965
1167 Syed, Z. A., Bouge, A. L., Byri, S., Chavoshi, T. M., Tang, E., Bouhin, H., van Dijk-Hard, I. F.,
1168 & Uv, A. (2012). A luminal glycoprotein drives dose-dependent diameter expansion of
1169 the Drosophila melanogaster hindgut tube. *PLoS Genet*, *8*(8), e1002850.
1170 https://doi.org/10.1371/journal.pgen.1002850
1171 Tang, W. J., Fernandez, J., Sohn, J. J., & Amemiya, C. T. (2015). Chitin is endogenously
1172 produced in vertebrates. *Curr Biol*, *25*(7), 897-900.
1173 https://doi.org/10.1016/j.cub.2015.01.058
1174 Tecle, E., Diaz-Balzac, C. A., & Bulow, H. E. (2013). Distinct 3-O-sulfated heparan sulfate
1175 modification patterns are required for kal-1-dependent neurite branching in a context-
1176 dependent manner in Caenorhabditis elegans. *G3 (Bethesda)*, *3*(3), 541-552.
1177 https://doi.org/10.1534/g3.112.005199
1178 Tomancak, P., Beaton, A., Weiszmann, R., Kwan, E., Shu, S., Lewis, S. E., Richards, S.,
1179 Ashburner, M., Hartenstein, V., Celniker, S. E., & Rubin, G. M. (2002). Systematic
1180 determination of patterns of gene expression during Drosophila embryogenesis. *Genome*
1181 *Biol*, *3*(12), RESEARCH0088. https://doi.org/10.1186/gb-2002-3-12-research0088
1182 Tonning, A., Hemphala, J., Tang, E., Nannmark, U., Samakovlis, C., & Uv, A. (2005). A
1183 transient luminal chitinous matrix is required to model epithelial tube diameter in the
1184 Drosophila trachea. *Dev Cell*, *9*(3), 423-430. https://doi.org/10.1016/j.devcel.2005.07.012
1185 Turnbull, J., Drummond, K., Huang, Z., Kinnunen, T., Ford-Perriss, M., Murphy, M., &
1186 Guimond, S. (2003). Heparan sulphate sulphotransferase expression in mice and
1187 Caenorhabditis elegans. *Biochem Soc Trans*, *31*(2), 343-348.
1188 https://doi.org/10.1042/bst0310343

1189 Uhlen, M., Bjorling, E., Agaton, C., Szigyarto, C. A., Amini, B., Andersen, E., Andersson, A. C.,
1190 Angelidou, P., Asplund, A., Asplund, C., Berglund, L., Bergstrom, K., Brumer, H.,
1191 Cerjan, D., Ekstrom, M., Elobeid, A., Eriksson, C., Fagerberg, L., Falk, R.,…Ponten, F.
1192 (2005). A human protein atlas for normal and cancer tissues based on antibody
1193 proteomics. *Mol Cell Proteomics*, *4*(12), 1920-1932.
1194 https://doi.org/10.1074/mcp.M500279-MCP200
1195 van den Boom, J., Heider, D., Martin, S. R., Pastore, A., & Mueller, J. W. (2012). 3'-
1196 Phosphoadenosine 5'-phosphosulfate (PAPS) synthases, naturally fragile enzymes
1197 specifically stabilized by nucleotide binding. *J Biol Chem*, *287*(21), 17645-17655.
1198 https://doi.org/10.1074/jbc.M111.325498
1199 Venkatachalam, K. V. (2003). Human 3'-phosphoadenosine 5'-phosphosulfate (PAPS) synthase:
1200 biochemistry, molecular biology and genetic deficiency. *IUBMB Life*, *55*(1), 1-11.
1201 https://doi.org/10.1080/1521654031000072148
1202 Venkatachalam, K. V., Akita, H., & Strott, C. A. (1998). Molecular cloning, expression, and
1203 characterization of human bifunctional 3'-phosphoadenosine 5'-phosphosulfate synthase
1204 and its functional domains. *J Biol Chem*, *273*(30), 19311-19320.
1205 https://doi.org/10.1074/jbc.273.30.19311
1206 Wang, S., Jayaram, S. A., Hemphala, J., Senti, K. A., Tsarouhas, V., Jin, H., & Samakovlis, C.
1207 (2006). Septate-junction-dependent luminal deposition of chitin deacetylases restricts
1208 tube elongation in the Drosophila trachea. *Curr Biol*, *16*(2), 180-185.
1209 https://doi.org/10.1016/j.cub.2005.11.074
1210 Weiszmann, R., Hammonds, A. S., & Celniker, S. E. (2009). Determination of gene expression
1211 patterns using high-throughput RNA in situ hybridization to whole-mount Drosophila
1212 embryos. *Nat Protoc*, *4*(5), 605-618. https://doi.org/10.1038/nprot.2009.55
1213 Wilkin, M. B., Becker, M. N., Mulvey, D., Phan, I., Chao, A., Cooper, K., Chung, H. J.,
1214 Campbell, I. D., Baron, M., & MacIntyre, R. (2000). Drosophila dumpy is a gigantic
1215 extracellular protein required to maintain tension at epidermal-cuticle attachment sites.
1216 *Curr Biol*, *10*(10), 559-567. https://doi.org/10.1016/s0960-9822(00)00482-6
1217 Wolfstetter, G., & Holz, A. (2012). The role of LamininB2 (LanB2) during mesoderm
1218 differentiation in Drosophila. *Cell Mol Life Sci*, *69*(2), 267-282.
1219 https://doi.org/10.1007/s00018-011-0652-3

1220 Wong, S. H., Hamel, L., Chevalier, S., & Philip, A. (2000). Endoglin expression on human
1221 microvascular endothelial cells association with betaglycan and formation of higher order
1222 complexes with TGF-beta signalling receptors. *Eur J Biochem*, *267*(17), 5550-5560.
1223 https://doi.org/10.1046/j.1432-1327.2000.01621.x
1224 Xia, B., Royall, J. A., Damera, G., Sachdev, G. P., & Cummings, R. D. (2005). Altered O-
1225 glycosylation and sulfation of airway mucins associated with cystic fibrosis.
1226 *Glycobiology*, *15*(8), 747-775. https://doi.org/10.1093/glycob/cwi061
1227 Yan, B., Zhang, Z. Z., Huang, L. Y., Shen, H. L., & Han, Z. G. (2012). OIT3 deficiency impairs
1228 uric acid reabsorption in renal tubule. *FEBS Lett*, *586*(6), 760-765.
1229 https://doi.org/10.1016/j.febslet.2012.01.038
1230 Yang, K., Liu, M., Feng, Z., Rojas, M., Zhou, L., Ke, H., & Pastor-Pareja, J. C. (2021). ER exit
1231 sites in Drosophila display abundant ER-Golgi vesicles and pearled tubes but no
1232 megacarriers. *Cell Rep*, *36*(11), 109707. https://doi.org/10.1016/j.celrep.2021.109707
1233 Zhang, L., Song, W., Li, T., Mu, Y., Zhang, P., Hu, J., Lin, H., Zhang, J., Gao, H., & Zhang, L.
1234 (2023). Redox switching mechanism of the adenosine 5'-phosphosulfate kinase domain
1235 (APSK2) of human PAPS synthase 2. *Structure*, *31*(7), 826-835 e823.
1236 https://doi.org/10.1016/j.str.2023.04.012
1237 Zhang, P., Zhang, L., Hou, Z., Lin, H., Gao, H., & Zhang, L. (2022). Structural basis for the
1238 substrate recognition mechanism of ATP-sulfurylase domain of human PAPS synthase 2.
1239 *Biochem Biophys Res Commun*, *586*, 1-7. https://doi.org/10.1016/j.bbrc.2021.11.062
1240 Zhang, Y., Foster, J. M., Nelson, L. S., Ma, D., & Carlow, C. K. (2005). The chitin synthase
1241 genes chs-1 and chs-2 are essential for C. elegans development and responsible for chitin
1242 deposition in the eggshell and pharynx, respectively. *Dev Biol*, *285*(2), 330-339.
1243 https://doi.org/10.1016/j.ydbio.2005.06.037
1244 Zhou, W., Chang, J., Wang, X., Savelieff, M. G., Zhao, Y., Ke, S., & Ye, B. (2014). GM130 is
1245 required for compartmental organization of dendritic golgi outposts. *Curr Biol*, *24*(11),
1246 1227-1233. https://doi.org/10.1016/j.cub.2014.04.008
1247 Zhu, X., Sen, J., Stevens, L., Goltz, J. S., & Stein, D. (2005). Drosophila pipe protein activity in
1248 the ovary and the embryonic salivary gland does not require heparan sulfate
1249 glycosaminoglycans. *Development*, *132*(17), 3813-3822.
1250 https://doi.org/10.1242/dev.01962

1251

Figure 1

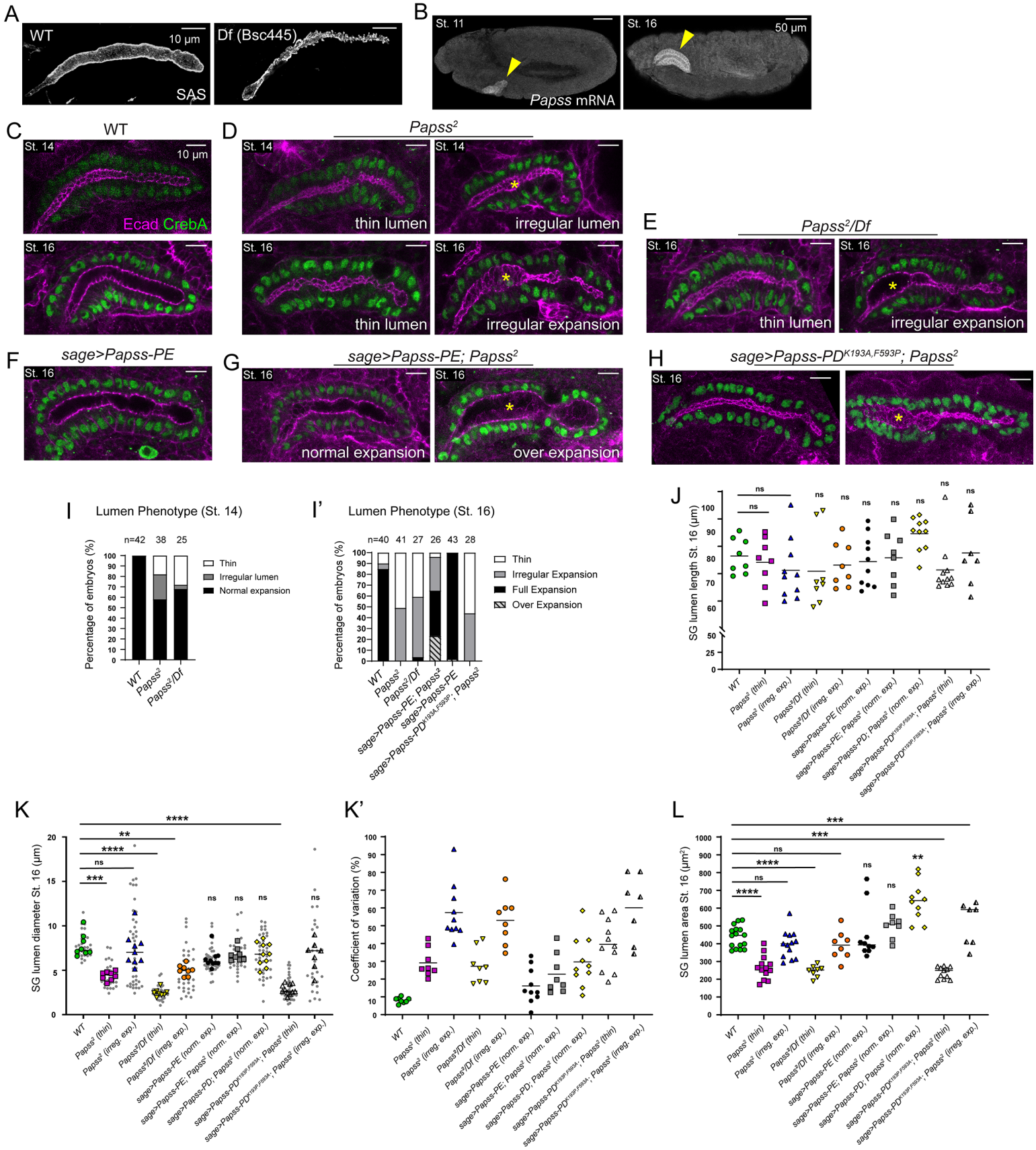
A
WT
10 µm
SAS
Df (Bsc445)
B
St. 11
St. 16
50 µm
Papss mRNA
C
WT
St. 14
10 µm
Ecad CrebA
St. 16
D
Papss2
St. 14
thin lumen
irregular lumen
St. 16
thin lumen
irregular expansion
E
Papss2/Df
St. 16
thin lumen
irregular expansion
F
sage>Papss-PE
St. 16
G
sage>Papss-PE; Papss2
St. 16
normal expansion
over expansion
H
sage>Papss-PDK193A,F593P; Papss2
St. 16
I
Lumen Phenotype (St. 14)
n=42 38 25
Percentage of embryos (%)
Thin
Irregular lumen
Normal expansion
WT
Papss2
Papss2/Df
I'
Lumen Phenotype (St. 16)
n=40 41 27 26 43 28
Percentage of embryos (%)
Thin
Irregular Expansion
Full Expansion
Over Expansion
WT
Papss2
Papss2/Df
sage>Papss-PE; Papss2
sage>Papss-PE
sage>Papss-PDK193A,F593P; Papss2
J
SG lumen length St. 16 (µm)
ns
WT
Papss2 (thin)
Papss2 (irreg. exp.)
Papss2/Df (thin)
Papss2/Df (irreg. exp.)
sage>Papss-PE (norm. exp.)
sage>Papss-PE; Papss2 (norm. exp.)
sage>Papss-PD; Papss2 (norm. exp.)
sage>Papss-PDK193P,F593A; Papss2 (thin)
sage>Papss-PDK193P,F593A; Papss2 (irreg. exp.)
K
SG lumen diameter St. 16 (µm)
****
**
****
ns
***
ns
ns
ns
ns
K'
Coefficient of variation (%)
L
SG lumen area St. 16 (µm2)
***
***
ns
****
ns
****
ns
ns
**

Figure 2

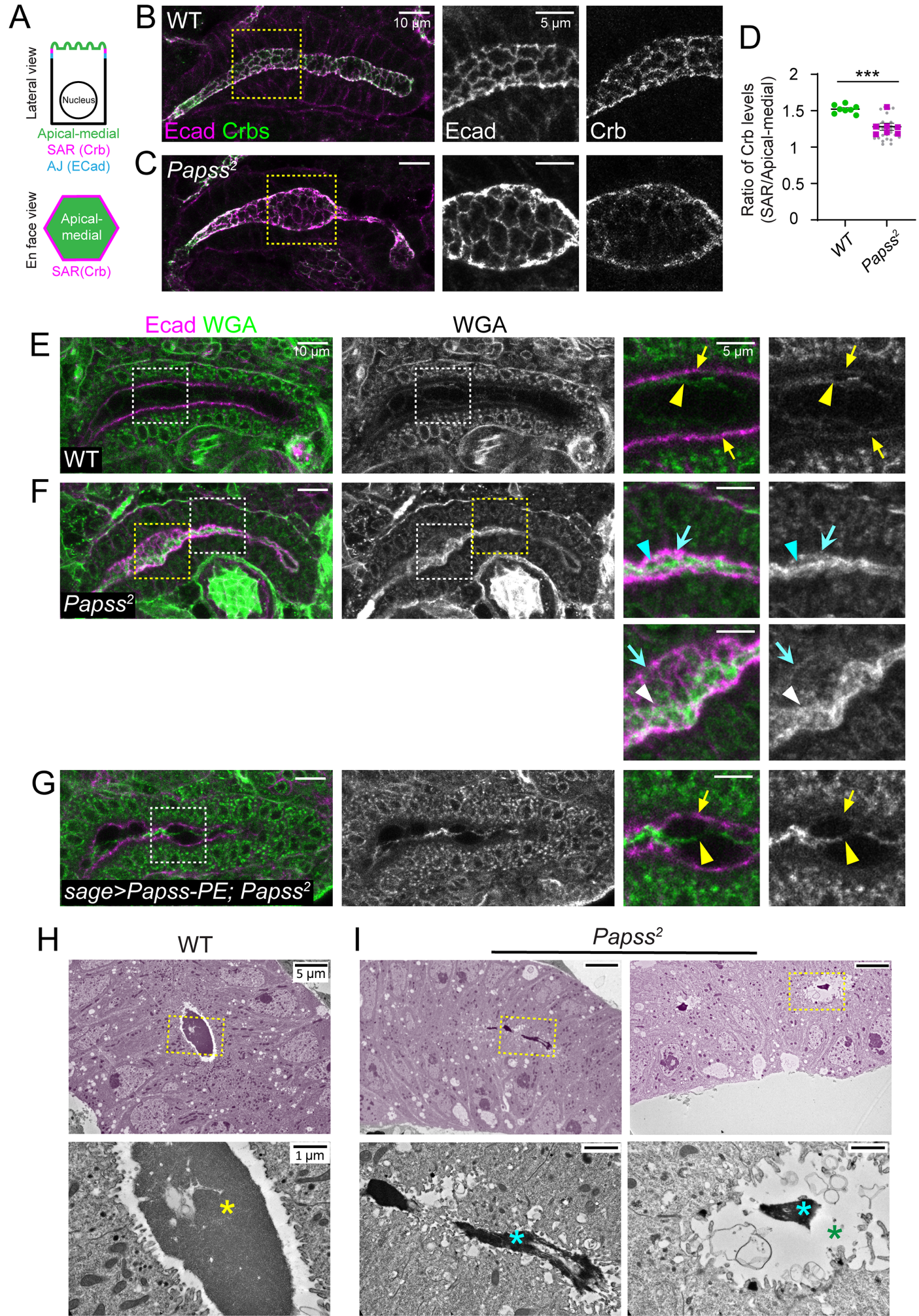
A
Lateral view
Nucleus
Apical-medial
SAR (Crb)
AJ (ECad)
En face view
Apical-medial
SAR(Crb)
B
WT
10 µm
5 µm
Ecad Crbs
Ecad
Crb
C
Papss2
D
Ratio of Crb levels (SAR/Apical-medial)
***
WT
Papss2
E
Ecad WGA
WGA
10 µm
5 µm
WT
F
Papss2
G
sage>Papss-PE; Papss2
H
WT
5 µm
1 µm
I
Papss2

Figure 3

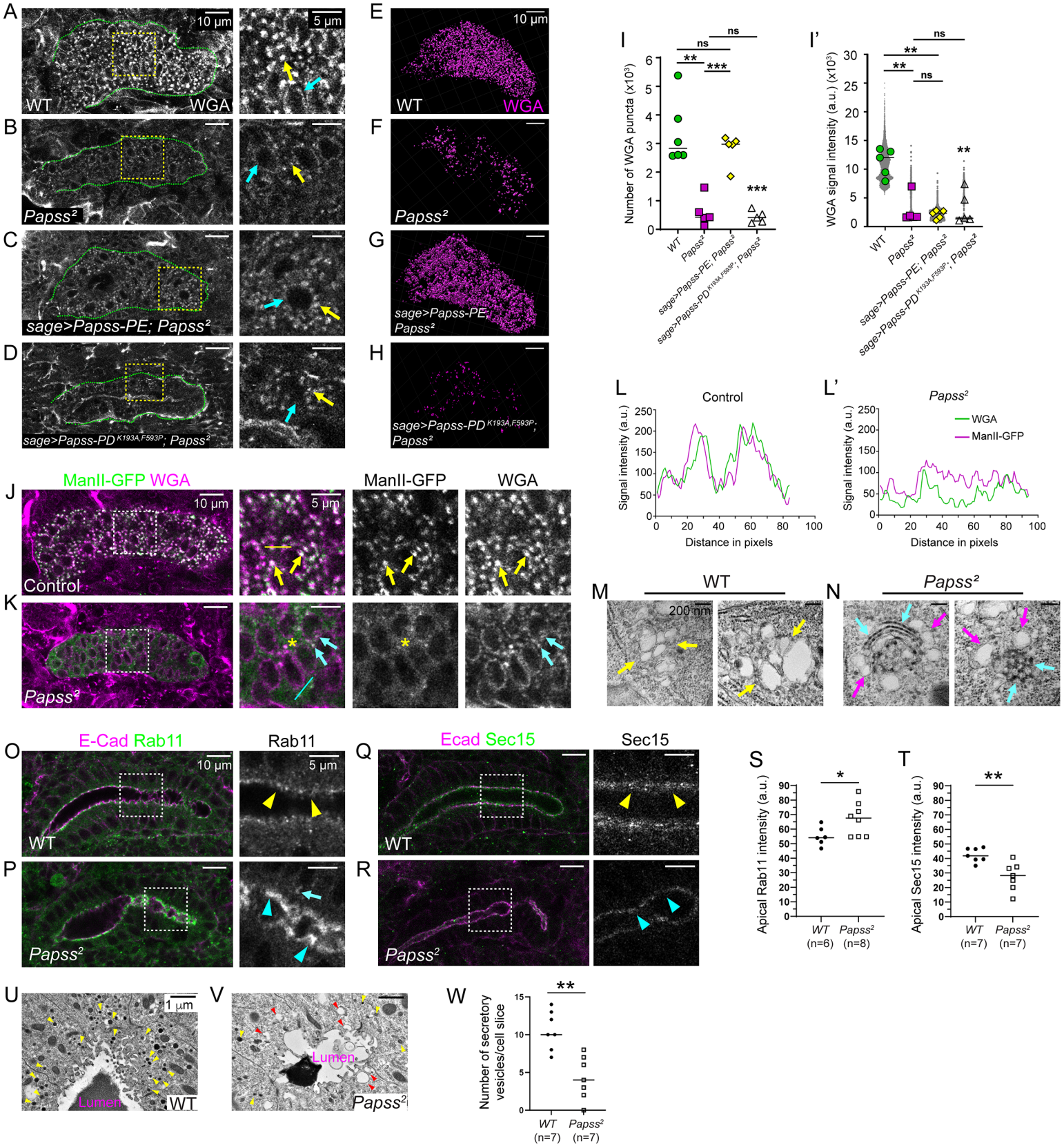
A
10 µm
5 µm
WT
WGA
B
Papss²
C
sage>Papss-PE; Papss²
D
sage>Papss-PD K193A,F593P; Papss²
E
10 µm
WT
WGA
F
Papss²
G
sage>Papss-PE; Papss²
H
sage>Papss-PD K193A,F593P; Papss²
I
Number of WGA puncta (x10³)
ns
**
***
WT
Papss²
sage>Papss-PE; Papss²
sage>Papss-PD K193A,F593P; Papss²
I'
WGA signal intensity (a.u.) (x10³)
L
Control
Signal intensity (a.u.)
Distance in pixels
L'
Papss²
WGA
ManII-GFP
J
ManII-GFP WGA
ManII-GFP
WGA
Control
K
Papss²
M
WT
200 nm
N
Papss²
O
E-Cad Rab11
Rab11
WT
P
Papss²
Q
Ecad Sec15
Sec15
WT
R
Papss²
S
Apical Rab11 intensity (a.u.)
WT (n=6)
Papss² (n=8)
T
Apical Sec15 intensity (a.u.)
WT (n=7)
Papss² (n=7)
U
1 µm
Lumen
WT
V
Lumen
Papss²
W
Number of secretory vesicles/cell slice
WT (n=7)
Papss² (n=7)

Figure 4

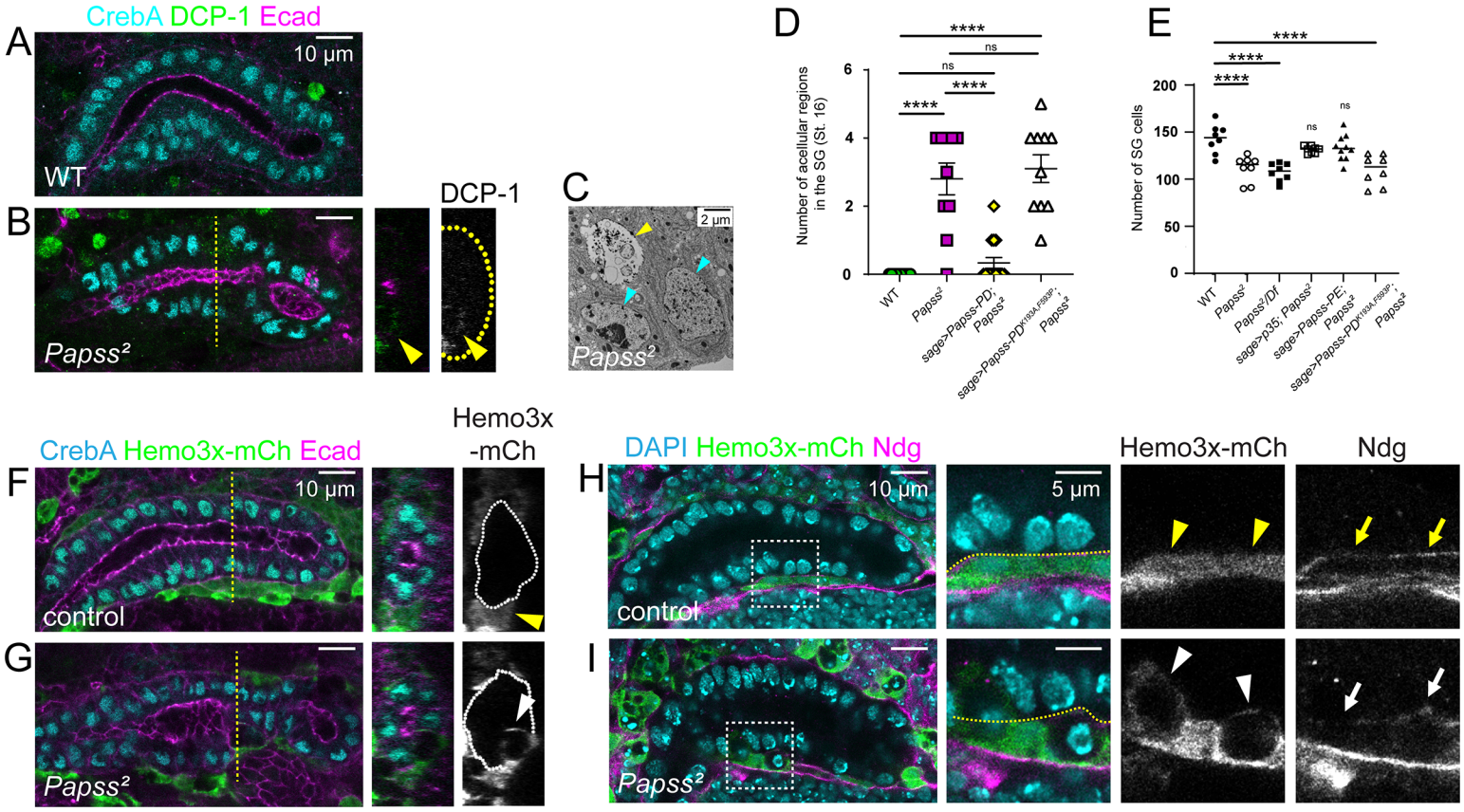
CrebA DCP-1 Ecad
A
10 µm
WT
B
Papss²
DCP-1
C
2 µm
Papss²
D
Number of acellular regions in the SG (St. 16)
****
ns
****
****
WT
Papss²
sage>Papss-PD; Papss²
sage>Papss-PD^K193A,F693P; Papss²
E
Number of SG cells
****
****
****
ns
ns
WT
Papss²
Papss²/Df
sage>p35; Papss²
sage>Papss-PE; Papss²
sage>Papss-PD^K193A,F693P; Papss²
CrebA Hemo3x-mCh Ecad
Hemo3x -mCh
F
10 µm
control
G
Papss²
DAPI Hemo3x-mCh Ndg
Hemo3x-mCh
Ndg
H
10 µm
5 µm
control
I
Papss²

Figure 5

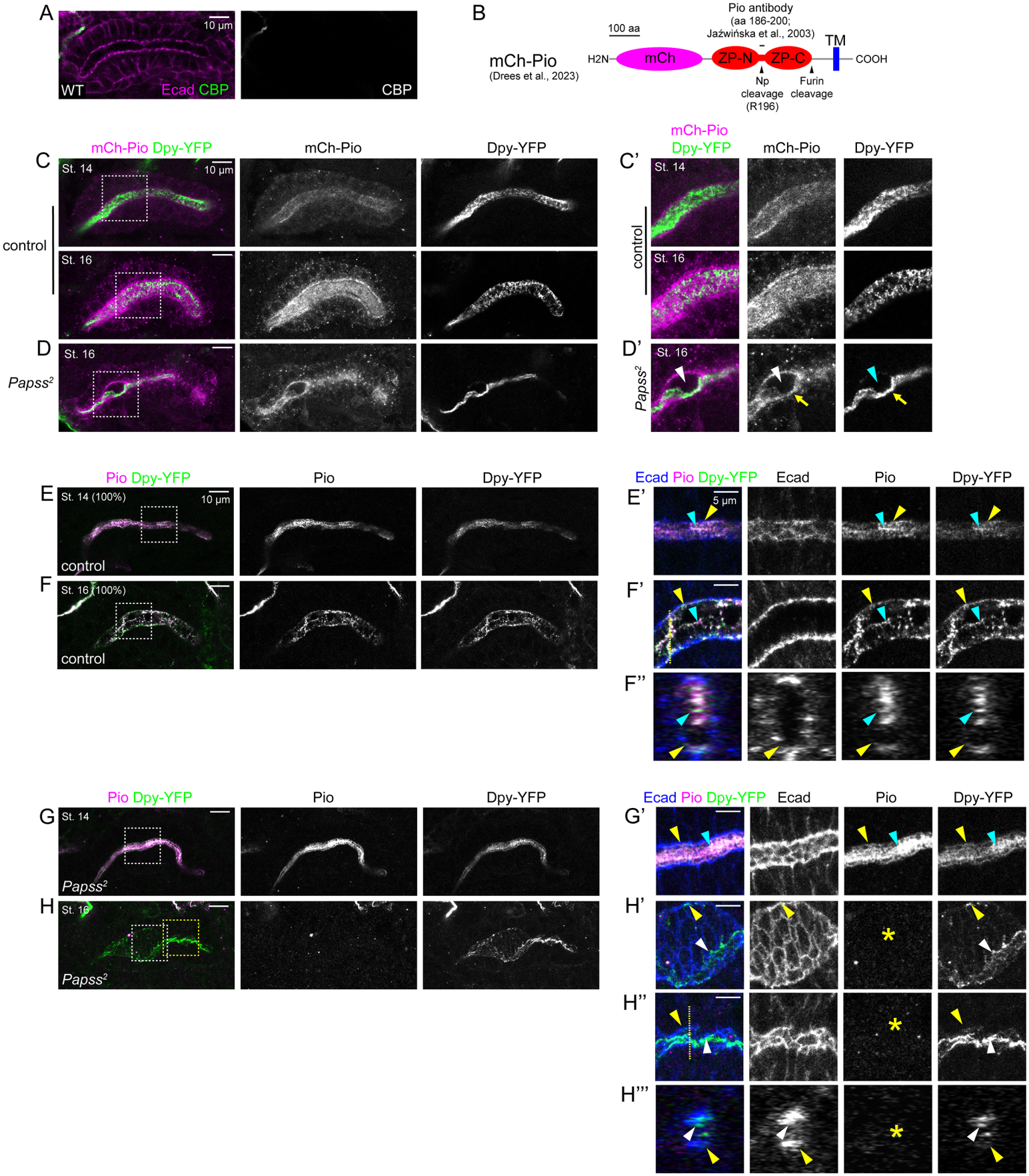
A
10 µm
WT
Ecad CBP
CBP
B
mCh-Pio
(Drees et al., 2023)
100 aa
H2N
mCh
Pio antibody
(aa 186-200;
Jaźwińska et al., 2003)
ZP-N
ZP-C
TM
COOH
Np
cleavage
(R196)
Furin
cleavage
C
mCh-Pio Dpy-YFP
mCh-Pio
Dpy-YFP
St. 14
10 µm
control
St. 16
D
St. 16
Papss2
C'
mCh-Pio
Dpy-YFP
mCh-Pio
Dpy-YFP
St. 14
control
St. 16
D'
St. 16
Papss2
E
Pio Dpy-YFP
Pio
Dpy-YFP
St. 14 (100%)
10 µm
control
F
St. 16 (100%)
control
E'
Ecad Pio Dpy-YFP
Ecad
Pio
Dpy-YFP
5 µm
F'
F''
G
Pio Dpy-YFP
Pio
Dpy-YFP
St. 14
Papss2
H
St. 16
Papss2
G'
Ecad Pio Dpy-YFP
Ecad
Pio
Dpy-YFP
H'
H''
H'''

Figure 6

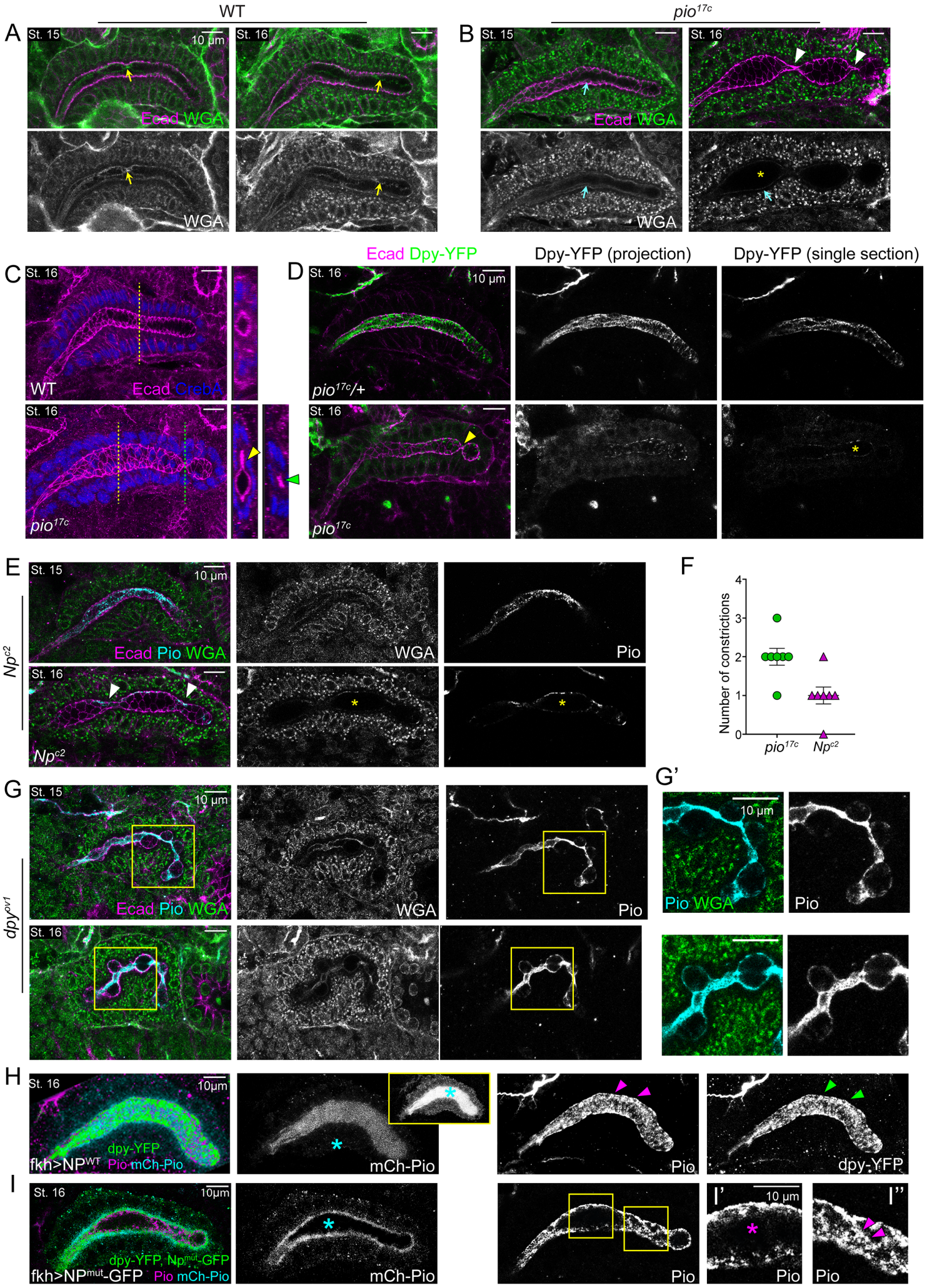
WT
pio17c
A
St. 15
10 µm
St. 16
Ecad WGA
WGA
B
St. 15
St. 16
Ecad WGA
WGA
C
St. 16
WT
Ecad CrebA
St. 16
pio17c
D
Ecad Dpy-YFP
Dpy-YFP (projection)
Dpy-YFP (single section)
St. 16
10 µm
pio17c/+
St. 16
pio17c
E
St. 15
10 µm
Ecad Pio WGA
WGA
Pio
Npc2
St. 16
Npc2
F
Number of constrictions
0
1
2
3
4
pio17c
Npc2
G
St. 15
10 µm
Ecad Pio WGA
WGA
Pio
dpyov1
St. 16
G'
10 µm
Pio WGA
Pio
H
St. 16
10µm
dpy-YFP
Pio mCh-Pio
fkh>NPWT
mCh-Pio
Pio
dpy-YFP
I
St. 16
10µm
dpy-YFP, Npmut-GFP
Pio mCh-Pio
fkh>NPmut-GFP
mCh-Pio
Pio
I'
10 µm
Pio
I''
Pio

Figure 7

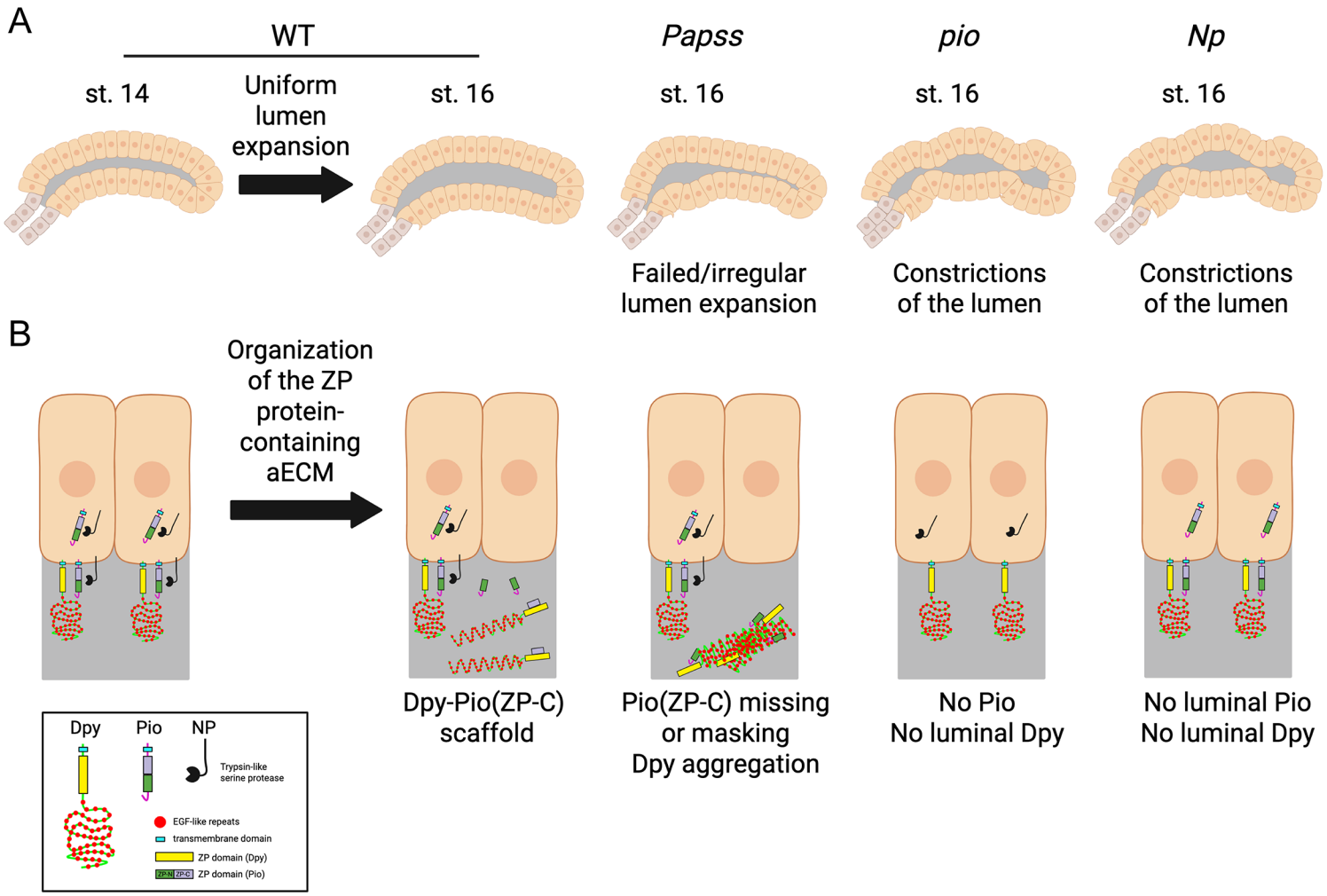
A
WT
st. 14
Uniform lumen expansion
st. 16
Papss
st. 16
Failed/irregular lumen expansion
pio
st. 16
Constrictions of the lumen
Np
st. 16
Constrictions of the lumen
B
Organization of the ZP protein-containing aECM
Dpy-Pio(ZP-C) scaffold
Pio(ZP-C) missing or masking Dpy aggregation
No Pio
No luminal Dpy
No luminal Pio
No luminal Dpy
Dpy
Pio
NP
Trypsin-like serine protease
EGF-like repeats
transmembrane domain
ZP domain (Dpy)
ZP-N
ZP-C
ZP domain (Pio)